Engineering graphene-based electrodes for optical neural stimulation

SCHOLARONE™
Manuscripts

Engineering graphene-based electrodes for optical neural stimulation

Artur Filipe Rodrigues[1,*], Ana P.M. Tavares[2], Susana Simões[1], Rui P.F.F. Silva[3], Tomas Sobrino[4], Bruno R. Figueiredo[3], Goreti Sales[2], Lino Ferreira[1,5,*]

[1] CNC – Center for Neurosciences and Cell Biology, University of Coimbra, 3000-517 Coimbra, Portugal

[2] BioMark@UC, Department of Chemical Engineering, Faculty of Sciences and Technology, University of Coimbra, 3030-790 Coimbra, Portugal

[3] Graphenest S.A., Edifício Vouga Park, 3740-070 Paradela do Vouga, Portugal

[4] NeuroAging Laboratory, Clinical Neurosciences Research Laboratory, Health Research Institute of Santiago de Compostela (IDIS), Santiago de Compostela, Spain

[5] Faculty of Medicine, Pólo das Ciências da Saúde, Unidade Central, University of Coimbra, 3000-354 Coimbra, Portugal

* Corresponding authors: afcdrodrigues@cnc.uc.pt ; lino@uc-biotech.pt

Abstract

Graphene-based materials (GBM) have been investigated in recent years with the aim of developing flexible interfaces to address a range of neurological disorders, where electrical stimulation may improve brain function and tissue regeneration. The recent discovery that GBM electrodes can generate an electrical response upon light exposure has inspired the development of non-genetic approaches capable of selectively modulate brain cells without genetic manipulation (i.e., optogenetics). Here, we propose the conjugation of graphene with upconversion nanoparticles (UCNP), which enable wireless transcranial activation using tissue-penetrating near-infrared (NIR) radiation. Following a Design of Experiments approach, we first investigated the influence of different host matrices and dopants commonly used to synthesize UCNPs in the electrical response of graphene. Two UCNP formulations achieving optimal enhancement of electric conductivity upon NIR activation at λ = 780 or 980 nm were identified. These formulations were then covalently attached to graphene nanoplatelets following selective hydroxyl derivatization. The resulting nanocomposites were evaluated *in vitro* using SH-SY5Y human neuroblastoma cells. NIR activation at λ = 980 nm promoted cell proliferation and downregulated neuronal and glial differentiation markers, suggesting the potential application of GBMs in minimally invasive stimulation of cells for tissue regeneration.

Keywords: Neuromodulation, graphene, near-infrared radiation, optoelectronic, tissue regeneration

1.   Introduction

Novel technologies to modulate the cellular and functional complexity of the brain have emerged with the aim of circumventing the limited efficacy of pharmacological therapies for the treatment of neurological disorders such as epilepsy, Alzheimer's (AD) and Parkinson's diseases (PD).[1] Despite the clinical implementation of medical devices delivering electrical pulses to control neuronal activity in specific regions of the brain,[2] significant adverse effects related to their long-term biocompatibility and limited spatial precision have hindered a more widespread use.[3–5] Multiple strategies have aimed to reduce device invasiveness by producing smaller electrodes, using flexible materials to improve their biocompatibility.[6–8] However, precise targeting of neuronal circuits to avoid overstimulating undesired cells and impairing physiological neuronal communication remains elusive.[9] Light has been demonstrated in preclinical studies to precisely target single cells and modulate neuronal circuits with unprecedented resolution.[10] However, these cells need to be genetically manipulated, posing significant ethical and safety concerns regarding the possible integration of undesired gene products after transfection.[11] In addition, this technique typically requires the use of visible light which poorly penetrates biological tissue, leading to the implantation of invasive light sources which may also generate heat and cause additional damage to the local tissue.[12]

Non-genetic transcranial activation of cells using light can be achieved using infrared and near-infrared (NIR) radiation, which can penetrate to deeper regions of the brain.[13–15] At these wavelengths, light may be absorbed by water and biomolecules, generating heat that may induce mechanical changes at the cell membrane and increase its capacitance, in a similar fashion to ultrasounds and magnetic fields.[16,17] However, excessive exposure to these stimuli (i.e., long exposure time or high power density) may instead suppress action potentials owing to heat-induced membrane hyperpolarization, which could be explained by the activation of K^+ channels.[18,19] These heat-mediated effects may also limit both spatial and temporal resolution of NIR activation.[20,21]

An ideal solution consists of the application of transducers capable of converting NIR radiation to electric current. Carbon nanomaterials including graphene and carbon nanotubes (CNT) are ideal candidates, owing to their exceptional electrical conductivity mediated by the network of π electrons resulting from the *sp²* hybridization of carbon atoms, as well as their flexibility and superior longevity in physiological milieu compared to other transparent materials, such as indium tin oxide (ITO) or poly(3,4-ethylenedioxythiophene) doped with polystyrene sulfonate (PEDOT:PSS).[22,23] Thin films composed by graphene or CNT in optogenetic preclinical models have enabled simultaneous imaging, electrophysiological recording and stimulation.[24–27] In particular, graphene-based materials (GBM) were demonstrated to minimize the generation of artifacts in magnetic resonance imaging (MRI).[28,29] Furthermore, GBMs exhibited superior biocompatibility compared to CNT,[30,31] and supported neuronal cell growth and differentiation.[32–34] The high capacitive charge injection of GBMs renders them suitable for long-term device operation with minimal cytotoxicity derived from electrochemical reactions.[35–40] GBM electrodes were recently shown to generate an electrical response upon light exposure.[26,41] This electrical

response was sufficient to elicit membrane depolarization and cardiomyocyte contraction *in vitro*, and depended on light intensity rather than wavelength.[41] However, this effect has only been observed in a limited number of wavelengths in the visible spectrum (485, 560, 630 nm). The electrical response of GBMs to other wavelengths remains to be demonstrated, particularly to NIR radiation.

Here, we have investigated the incorporation of lanthanide-doped upconversion nanoparticles (UCNP) to improve the electrical response of GBM electrodes to low-power NIR radiation for brain stimulation. UCNPs have been explored in transcranial optogenetic stimulation due to their ability of absorbing NIR radiation and releasing visible light with minimal photobleaching and heat-mediated photodamage.[15,42,43] These nanocrystals are also more suitable for biomedical applications than NIR-responsive quantum dots, owing to their biocompatibility and chemical versatility to tune their optical properties.[44] While several studies have shown that UCNPs can dramatically improve the sensitivity of graphene-based photodetectors to NIR radiation,[45–48] it remains to be investigated whether lanthanide composition, which determines the optical properties of UCNPs, can be leveraged to further improve charge transfer from UCNPs to graphene and improve its electrical conductivity. Furthermore, to the best of our knowledge, most of graphene-UCNP photodetectors reported thus far were prepared by exploiting either non-covalent interactions,[45–47] or electrostatic interactions between the positively charged lanthanides of UCNPs and the negatively charged oxygen functionalities of GBMs.[48–50] Although a previous study has reported the preparation of graphene-UCNP composites after covalent immobilization of silica-coated UCNPs onto polymer-coated GBMs,[51] these were employed in NIR-mediated photothemal and photodynamic therapies, and not for brain stimulation. The effects of NIR radiation on cells interfacing with graphene-UCNP composites also remain unknown.

In this work, graphene-UCNP electrodes were engineered by rational design of UCNPs with different combinations of lanthanides, with the aim of maximizing the amount of generated current upon exposure to NIR radiation. After selecting 2 optimal UCNP formulations, graphene-UCNP nanocomposites were generated by selective hydroxyl derivatization of graphene nanoplatelets, and evaluated *in vitro* using SH-SY5Y human neuroblastoma cells as a model of neuronal-like cells.

2.   Experimental

Preparation of GBM electrodes. Electrodes were prepared as previously described.[52,53] Briefly, graphene nanoplatelets provided from Graphenest were mixed with sodium carboxymethoxyl cellulose (CMC, average Mw ~ 250 kDa, Sigma Aldrich), dissolved in a mixture of milliQ ultrapure water and ethanol (Fisher Chemical) at a volume ratio of 1:1 for 1 h at room temperature. The ink was formulated at a graphene:CMC mass ratio of 9:1 and mixed in a rotary evaporator for 1 h at 2000 rpm. Electrodes were screen-printed onto a polyethylene terephthalate (PET) foil with 100 μm of thickness, using a custom metallic frame with a 100T screen mesh designed to match the

dimensions of commercial screen-printed electrodes. The graphene-based ink was used to print the counter and working (diameter = 5 mm) electrodes using 5 printing steps to avoid defects that could compromise their conductivity. The reference electrode was printed in one step using a commercial silver ink (Henkel, ref: Loctite EDAG PF-410 E&C), while a blue polymer was applied on top of the electrode channels as the dielectric component (SunChemical Gwent Electronic Materials, ref: D50706P3). After printing, the electrodes were cured in an oven at 100ºC for 30 min.

Electrochemical characterization of GBM electrodes. The screen-printed 3-electrode system was fitted to a spectroelectrochemical cell (Metrohm DropSens, ref: DRP-Transcell 70066) for electrochemical measurements under laser irradiation. A laser fiber was attached at a fixed height on top of the spectroelectrochemical cell, resulting in an incident beam diameter of 2 mm. Laser power and wavelength was adjusted using a controller equipped with diodes at 3 different wavelengths (405, 780, 980 nm), and calibrated using a power sensor (Thorlabs S310C). The electrodes were covered with 60 µL of phosphate buffer saline (PBS, Sigma Aldrich) prepared at 0.01 M, pH 7.4 in milliQ ultrapure water. Electrochemical measurements were performed using a PGSTAT204 potentiostat equipped with a FRA32M frequency response analyzer module (Metrohm Autolab). Data were processed using Nova software (Metrohm Autolab, version 2.1.5). Electrochemical impedance spectroscopy was performed with a sinusoidal potential perturbation at an amplitude of 10 mV, in order to record the impedance over a frequency range of 0.1 to 10000 Hz at a rate of 10 points per decade. Cyclic voltammetry was performed in a range from -0.6 to +0.6 V at a scan rate of 50 mV s^{-1} over 10 cycles to stabilize the recorded signal. Only the last scan was used to determine the area under the voltammogram curve (AUC) in order to calculate electrode capacitance and cathodic charge storage capacity (CSC):

$$Capacitance\ (\mu F\ cm^{-2}) = \frac{|AUC\ (\mu A.V)|}{2 \times 0.05\ V\ s^{-1} \times (0.6\ V - (-0.6\ V)) \times Electrode\ area\ (cm^2)}$$

Cathodic CSC was derived from the difference between the absolute and the mathematical values of the AUC, in order to obtain the value corresponding to the negative sweep.[35] This was divided by the scan rate and normalized by electrode area:

$$CSC\ (\mu C\ cm^{-2}) = \frac{|AUC\ (\mu A.V)| - AUC\ (\mu A.V)}{0.05\ V\ s^{-1} \times Electrode\ area\ (cm^2)}$$

Design of Experiments. Multivariate analysis of lanthanide dopants on the electrical response of graphene nanoplatelets to NIR radiation was performed using JMP software (version 13, SAS). A library of UCNPs was generated using a Definitive Screening Design, with Yb (0 – 20%), Nd (0 – 2%), Tm (0 – 0.5%), Er (0 – 3%), and Sm (0 – 5%) set as 3-level continuous factors (% mol), while the host nanocrystal was set as a 2-level categorical variable (NaYF$_4$ or NaGdF$_4$). Two additional UCNP formulations (R-04, FR-12) were added as common formulations reported in the

literature (NaYF$_4$:Yb,Er and NaYF$_4$:Yb,Tm, respectively), while FR-13 consisted of a pure NaYF$_4$ nanocrystal lacking any dopants.

Each of the 21 UCNP formulations (0.5 mg) was drop-casted onto the working area of the graphene electrode and dried in an oven at 60ºC for 2 h. Electrochemical response of each graphene-UCNP combination in PBS 1x was evaluated as described above, using NIR radiation (30 mW cm^{-2}) at λ = 780 nm and/or 980 nm, depending on the incorporation of Nd and/or Yb, respectively. The difference in the calculated capacitance of each electrode with or without NIR radiation (n = 2-3 electrodes per UCNP formulation) was fitted to a standard least squares model, using leverage plots to analyze the main effects of each variable and their first-order interactions. Non-significant effects ($p > 0.05$) were progressively excluded from the model until only statistically significant effects remained in the model as determined by ANOVA.

Synthesis of silane-coated UCNPs. Lanthanide-doped nanocrystals were prepared by solvothermal synthesis as previously reported.[54] Yttrium(III), gadolinium(III), ytterbium(III), neodymium(III), thulium(III), erbium(III), and samarium(III) acetate salts (Sigma Aldrich) were dissolved at different ratios to a total of 0.5 mmol of metallic acetates, in a mixture of 18 mL oleic acid (Alfa Aesar) and 45 mL 1-octadecene (Acros Organics) under an inert nitrogen atmosphere. The mixture was stirred under vacuum at 120ºC for 1 h, in order to remove acetic acid and minimize the water content in the crystal lattice which could quench UCNP luminescence.[55] After cooling down to 50ºC, 30 mL of methanol (Fisher Chemical) containing 20 mmol ammonium fluoride (740.8 mg, Acros Organics) and 12.5 mmol sodium hydroxide (500 mg, Merck Sigma) were added to the mixture and stirred for 30 min. Methanol was distilled after increasing the reaction temperature to 100ºC and flushing with nitrogen gas. The reaction temperature was progressively increased to 300ºC under nitrogen gas flow, in order to nucleate the nanocrystals. After 90 min at 300ºC, the reaction mixture was allowed to cool down to 50ºC and washed with acetone (Fisher Chemical), followed by centrifugation at 6000 rpm (4629 g) for 6 min to separate the nanocrystals. The resulting pellet was redispersed in cyclohexane (Fluka) and washed 2 more times with ethanol (Fisher Chemical). The purified core UCNPs, dispersed in cyclohexane, were added to a mixture of 18 mL oleic acid and 45 mL 1-octadecene containing 0.45 mmol yttrium(III) acetate (119.72 mg), which had been previously stirred under vacuum at 120ºC for 30 min. The mixture was stirred for 30 min at 80ºC. When the reaction temperature lowered to 50ºC, 30 mL methanol containing 17.5 mmol ammonium fluoride (648.2 mg) and 10.9 mmol sodium hydroxide (437.6 mg) were added to the mixture as described above. A NaYF$_4$ shell was crystalized on the surface of core UCNPs after evaporating the methanol from the mixture and stirring for 90 min at 300ºC under an inert atmosphere. The resulting core-shell nanocrystals were purified by centrifugation and washed with acetone and ethanol, as described above. The resulting oleic acid-coated nanocrystals were finally dispersed in cyclohexane.

Water-dispersible UCNPs were obtained after ligand exchange to replace oleic acid with citric acid.[54] Briefly, 580 mg UCNPs dispersed in cyclohexane were added to a mixture of 40 mL 1,2-dichlorobenzene (Acros Organics) and 40 mL N, N'-dimethylformamide (Fisher Chemical), followed by the addition of 0.5 g citric acid (Merck Sigma). After stirring for 24 h, the hydrophilic

UCNPs were precipitated in the mixture after the addition of diethyl ether (Fisher Chemical) and centrifugation at 6000 rpm (4629 g) for 6 min. The resulting pellet was redispersed in milliQ water and washed thrice with acetone, followed by centrifugation at 6000 rpm (4629 g) for 6 min. Silanization was performed by mixing citrate-coated UCNPs (100 mg) dispersed in 50 mL methanol (Fisher Chemical) with 20 µL (3-aminopropyl)triethoxysilane (85 µmol, Sigma Aldrich) and 40 µL (3-azidopropyl)triethoxysilane (160 µmol, Gelest Inc.) for 12 h at room temperature. Then, 50 mL glycerol (Fisher Chemical) were added to the mixture, which was evaporated in a rotary evaporator at 40ºC to remove the methanol. Temperature progressively increased to 95ºC to promote water evaporation and silane condensation under vacuum for 2 h. Silanized UCNPs (UCNPs@NH$_2$/N$_3$) were flocculated in an aqueous solution of 70% (v/v) acetone and centrifuged at 6000 rpm (4629 g) for 6 min. The resulting pellet was redispersed in milliQ water and washed 2 more times with 70% acetone. The final UCNP dispersion was obtained in water.

Conjugation of UCNPs with graphene nanoplatelets. Graphene nanoplatelets (100 mg, Graphenest) were dispersed in 40 mL anhydrous tetrahydrofuran (Sigma Aldrich), followed by the slow addition of 700 µL triethylamine (5 mmol, Alfa Aesar) and 650 µL acryloyl chloride (8 mmol, Merck Sigma) while the reaction flask was kept in an ice bath under nitrogen atmosphere. After stirring for 1 h, the ice bath was removed and the mixture was left stirring at room temperature for 18 h. The resulting mixture was purified by solubilizing the resulting triethylamine hydrochloride salt in chloroform (Fisher Chemical), followed by centrifugation at 9000 rpm (10414 g) for 10 min. The obtained pellet was redispersed in tetrahydrofuran (Fisher Chemical) before a new washing step with acetone. Acrylated graphene was dispersed in tetrahydrofuran until its conjugation with UCNPs. After evaporating the solvent, acrylated graphene was redispersed in 20 mL anhydrous DMSO (Alfa Aesar), followed by the addition of 100 mg UCNPs@NH$_2$/N$_3$. The mixture was stirred for 48 h at 65ºC. The resulting composites were precipitated with ethyl acetate and centrifuged at 9000 rpm (10414 g) for 10 min. The pellet was redispersed in milliQ water and underwent new washing steps with ethyl acetate followed by acetone.

Quantification of vinyl groups after acrylation of graphene. Vinyl groups were quantified after covalent functionalization with a fluorescent probe via thiol-Michael addition. GBMs (0.1 mg) were diluted in 198 µL DMSO, followed by the addition of 2 µL FAM Thiol (BioActs) dissolved in DMSO at 20 mM. A calibration curve was obtained after preparing standard solutions of FAM Thiol in DMSO (25 – 200 µM). After reacting for 2 h at room temperature, all samples were centrifuged at 13000 g for 10 min. The resulting pellets were redispersed in 200 µL DMSO and transferred to a 96-well black plate (100 µL/well). Fluorescence intensity was recorded using a Synergy H1 plate reader (Biotek) set with excitation wavelength = 492 nm and emission wavelength = 519 nm.

Quantification of primary amines after conjugation of UCNPs. Primary amines in UCNPs were quantified by measuring the fluorescence of the product obtained from their reaction with fluorescamine. Each sample (0.1 mg) was diluted in 175 µL PBS 1x and mixed with 25 µL fluorescamine (Sigma Aldrich) dissolved in acetone at a concentration of 6 mg mL^{-1}. A calibration

curve was obtained after preparing serial dilutions (1:2) of glycine in PBS 1x (1.95 – 62.5 µM). All samples were then transferred to a 96-well black plate (100 µL/well) and fluorescence intensity was recorded using a Synergy H1 plate reader (Biotek) set with excitation wavelength = 400 nm and emission wavelength = 460 nm.

Inductively coupled plasma mass spectroscopy. Quantification of yttrium in UCNPs and graphene-UCNP nanocomposites was performed by ICP-MS at the University of Santiago de Compostela, Spain. Samples were prepared by freeze-drying 100 µg of each nanomaterial, followed by digestion in 70% (w/v) nitric acid. All samples were reconstituted in 10 mL of 2% (w/v) nitric acid and analyzed using an Agilent 7700x ICP-MS system (Agilent).

Nanoparticle size and charge. Hydrodynamic diameter and ζ-potential were measured by dynamic light scattering (DLS) using a ZetaPALS Analyzer (Brookhaven Instruments Corporation). GBMs and UCNPs were diluted in 1.5 mL of milliQ ultrapure water containing 1 mM KCl (Merck Sigma) at a concentration of 0.1 mg mL^{-1}. All size measurements were performed using the same incident laser power, whereas ζ-potential measurements were performed by maximizing incident laser power for each sample. Reported values for each sample correspond to the average of 5 measurements.

Transmission electron microscopy. Each sample was diluted in 30 µL of milliQ ultrapure water (1 mg mL^{-1}). A droplet of each sample was placed on Formvar/carbon film-coated mesh nickel grids (Electron Microscopy Sciences) and allowed to adhere for 10 min. Excess liquid was removed with filter paper. Image acquisition was carried out on a JEOL JEM-1400 electron microscope operating at 120 kV, equipped with an Orious 1100W CCD digital camera. Nanoparticle size distribution was analyzed by manual counting on several TEM images using ImageJ (version 1.51, NIH).

X-ray photoelectron spectroscopy. Chemical composition of GBMs and UCNPs was studied by XPS at CEMUP (Materials Center of the University of Porto, Portugal). Samples were prepared by deposition of 30 µg of each nanomaterial (1 mg mL^{-1}) onto 5 x 5 silicon wafers (Ted Pella), which were left to dry overnight. XPS spectra were recorded using a Kratos Axis Ultra HAS spectrometer equipped with a monochromatic Al Kα source of 1486.7 eV. Survey spectra were acquired with a pass energy of 160 eV, 1 eV step size, and 200 ms dwell time. High-resolution C1s, O1s, N1s, Si2p, Y3d, and Gd3d were acquired with a pass energy of 40 eV, 0.1 eV step size, and 1500 ms dwell time. All spectra were processed using CasaXPS software (version 2.3, Casa Software Ltd). High-resolution spectra were charge-corrected by shifting all peaks to the adventitious carbon peak in the C1s spectra, which was set at 284.6 eV. Each spectrum was deconvoluted into different components after subtracting the background using the Shirley algorithm. Each component was assigned according to NIST and LaSurface XPS databases. All components in C1s and O1s spectra were deconvoluted using a Gaussian:Lorentzian (70:30) function, except the peak attributed to carbon-carbon bonds, which was fitted by an asymmetric

Lorentzian function. Apart from the satellite π – π* contribution in C1s spectra, all peaks in each spectrum were constrained to the same full width at half-maximum value.

Cell culture. SH-SY5Y human neuroblastoma cells were purchased from the European Collection of Authenticated Cell Cultures (ECACC cat. no. 94030304), and maintained in DMEM medium (Sigma Aldrich) containing 6 mM L-glutamine (Gibco), 5 mM HEPES (Sigma Aldrich), 3.7 g L^{-1} sodium bicarbonate (Sigma Aldrich), and 0.11 g L^{-1} sodium pyruvate (Sigma Aldrich), and supplemented with D-(+)-glucose (Fluka) at a concentration of 4.5 g L^{-1}, 10% (v/v) fetal bovine serum (FBS, Life Technologies), and 1% (v/v) penicillin-streptomycin (Lonza).[56] Cells were grown at 37°C in a humidified chamber with an atmosphere containing 5% CO_2. Cells were passaged after trypsinization using trypsin-EDTA 0.1% (Gibco) when they achieved 80-90% confluency (every 3-4 days). All experiments were performed using cells with passage numbers between 3 and 8.

Cytotoxicity assays. SH-SY5Y cells (6000 cells/well) were seeded in 96-well plates 24 h before nanomaterial treatments. Nanomaterial dispersions were prepared shortly before exposure over a range of concentrations between 5 and 200 µg mL^{-1} (20 – 400 µg mL^{-1} for UCNPs). Sterile-filtered DMSO (Sigma Aldrich) diluted in cell culture medium (10% v/v) was used as a positive control. After 4 h of incubation in serum-free DMEM, cells were replenished with medium containing 10% (v/v) FBS. Cytotoxicity was analyzed 24 h after nanomaterial treatment.
In order to evaluate nanomaterial interactions in cells bearing a neuronal-like phenotype, SH-SY5Y cells were cultured for 3 days in a differentiation medium which differs from the medium described above by the decrease in D-(+)-glucose and FBS to concentrations of 0.9 g L^{-1} and 1% (v/v), respectively, as well as the addition of 10 µM retinoic acid (Sigma Aldrich) dissolved in DMSO.[56] Nanomaterial exposure was performed as described above, 48 h after seeding 10000 cells/well in 96-well plates.

Alamar Blue assay. Resazurin (Sigma Aldrich) was dissolved at a stock concentration of 0.2 mg mL^{-1}. Cells previously exposed to nanomaterials in 96-well plates were treated with 10 µL resazurin and incubated for 2 h at 37°C. After centrifuging the plates at 4000 rpm for 20 min, 50 µL of each supernatant were transferred to a 96-well black plate. Metabolic activity of SH-SY5Y cells was measured by the reduction of resazurin to a fluorescent product, whose fluorescence intensity was recorded using a Synergy H1 plate reader (Biotek) set with excitation wavelength = 560 nm and emission wavelength = 590 nm.

Propidium iodide staining. Cells previously treated to nanomaterials in 96-well plates were stained with Hoeschst H33342 and propidium iodide (PI), both (Sigma Aldrich) at 1 µg mL^{-1} in cell culture medium. Cell death was quantified by live cell imaging using the InCell Analyzer 2200 microscope (GE Healthcare). Seven fields per well were acquired with a 20x objective using the laser autofocus method on the following channels: DAPI/Hoeschst 33342 (exposure: 0.6 s, excitation/emission: 390/435 nm), Texas Red/PI (exposure: 0.2 s, excitation/emission: 575/620

nm). TIFF images produced for each channel were processed using the InCell Investigator software (GE Healthcare). Cells were identified using the top-hat method in the DAPI channel (minimum area = 80 µm^2, sensitivity = 93), followed by classification of viability according to the cell nuclei. Dead cells were identified by nuclear condensation (Nuc Intensity CV < 0.4) and co-localization with PI staining, determined by pseudo-segmentation in the Texas Red channel.

DCF-DA assay. SH-SY5Y cells (8000 cells/well) were seeded in 96-well plates 24 h before pre-treatment with 20 µM H$_2$DCF-DA (Invitrogen) in PBS 1x for 45 min. GBM dispersions were prepared shortly before exposure at 10, 20 and 50 µg mL^{-1}. Hydrogen peroxide (Panreac) diluted in cell culture medium (1 mM) was used as a positive control. Cells were washed with PBS and incubated with the treatments for 4 h. The medium was transferred to a 96-well black plate, and fluorescence intensity was recorded using a Synergy H1 plate reader set with excitation wavelength = 488 nm and emission wavelength = 530 nm. The remaining cells were stained with Hoeschst H33342 and imaged using the InCell Analyzer 2200 microscope. Seven fields per well were acquired with a 20x objective using the laser autofocus method on the following channels: DAPI/Hoeschst 33342 (exposure: 0.6 s, excitation/emission: 390/435 nm), FITC/GFP (exposure: 0.4 s, excitation/emission: 475/511 nm).

Preparation of graphene-based substrates for cell culture. Graphene-based substrates were freshly prepared for cell culture by spray coating 250 µL of each dispersion in tetrahydrofuran (40 mg mL^{-1}) onto 1.3 x 1.3 cm PET films (A = 1.69 cm^2). These substrates were fitted into 24-well plates and dried at 60ºC for 1 hour. Finally, they were exposed to UV radiation (30 mW cm^{-2}) for 1 min for sterilization prior to use in cell culture.

Cell counting. SH-SY5Y cells (30000 cells/well) were seeded onto graphene-based substrates placed in a 24-well plate 24 h before treatment. Cells were exposed to NIR radiation at λ = 780 or 980 nm at different irradiances (0.1 – 1.8 W cm^{-2}) and exposure times (5 – 60 min). After 24 h, cells were stained with DAPI (1 µg mL^{-1}; Sigma Aldrich) for 5 min and washed with PBS 1x. The graphene-based films were removed from the plate, blot dried, and transferred to glass slides for mounting with fluorescence mounting medium (Dako). Films were imaged using the InCell Analyzer 2200 microscope, set with a 20x objective. A large area comprised of 36 fields was acquired in each substrate using the laser autofocus method on the following channels: DAPI/Hoeschst 33342 (exposure: 1.0 s, excitation/emission: 390/435 nm), FITC/GFP (exposure: 0.8 s, excitation/emission: 475/511 nm). The green channel was used to subtract film and cell autofluorescence from DAPI images. Cell density was calculated from the number of DAPI nuclei in each field, while cytotoxicity was estimated by measuring nuclei size to account for nuclear condensation.

Cell cycle analysis. SH-SY5Y cells (40000 cells/well) were seeded onto graphene-based substrates placed in a 24-well plate. After 24 h, cells were exposed to NIR radiation at λ = 780 or 980 nm (100 mW cm^{-2}) for 5 min. Cells were trypsinized 48 h after irradiation and washed with

PBS before fixation in ice-cold ethanol (70% v/v) for 30 min at 4ºC. The permeabilized cell suspensions were vortexed to avoid clumping and washed with PBS, followed by centrifugation at 350 g for 5 min. This step was repeated twice before treatment with 30 µL RNase A (100 µg mL^{-1}, Sigma Aldrich) for 20 min. Cells were washed with PBS and stained with 100 µL propidium iodide (50 µg mL^{-1}, Invitrogen) for 5 min. Cells were finally washed in PBS and re-suspended for analysis by flow cytometry, using a BD Accuri C6 flow cytometer (BD Biosciences), equipped with 488 nm and 640 nm lasers. Cell cycle was characterized based on the amount of nuclear DNA stained with PI, whose fluorescence was quantified using the 675/25 filter. Data were processed using FlowJo software (version X.0.7, FlowJo LLC).

Immunocytochemistry. An aliquot of trypsinized SH-SY5Y cells used for cell cycle analysis was transferred to a µ-Slide 8-well (IBIDI) chambered coverslip (25000 cells/well). Cells were gently rinsed with PBS 1x 24 h after seeding and fixed with 4% paraformaldehyde (Alfa Aesar) for 10 min. Cells were washed 3 times with PBS for 5 min each, followed by permeabilization with 0.3% Triton X-100 (Fluka) in PBS for 10 min. Cells were washed again with PBS thrice before blocking with 1% BSA (Sigma Aldrich) and 0.3 M glycine (Acros Organics) in PBS for 1 h. Cells were then incubated for 1 h with mouse anti-doublecortin (1:50; Santa Cruz, cat. no. sc-271390), goat anti-GFAP (1:1000; Abcam, cat. no. ab53554), and rabbit anti-Ki67 (1:400; Cell Signaling, cat. no. 1679129S), diluted in PBS 1x containing 1% BSA. After a washing step with PBS (3 x 5 min) to remove the primary antibody cocktail, cells were incubated for 1 h with Alexa Fluor 488 donkey anti-mouse IgG (Invitrogen, cat. no. A21202), Alexa Fluor 555 donkey anti-goat IgG (Invitrogen, cat. no. A21432), and Alexa Fluor 647 donkey anti-rabbit IgG (Invitrogen, cat. no. A31573), all diluted 1:1000 in PBS 1x containing 1% BSA. After another washing step with PBS 1x (3 x 5 min), cell nuclei were stained with DAPI (1 µg mL^{-1}) for 5 min and washed with PBS 1x before imaging using a Zeiss LSM 710 confocal microscope, equipped with an Apochromat 40x/1.4 objective. Images were analyzed in ImageJ (version 1.51, NIH) to measure fluorescence intensity levels of each cell marker using the Analyze Particles built-in function.

Statistical analysis. All experiments were analyzed using GraphPad Prism software (version 7, GraphPad Inc.). Data were analyzed using 1- or 2-way ANOVA tests with *post hoc* multiple comparisons test, provided statistical significance was obtained when $p < 0.05$.

3.   Results and Discussion

3.1. Electrochemical response of graphene-based electrodes to NIR radiation

The electrochemical response of graphene to light was initially investigated by performing cyclic voltammetry (CV) and electrochemical impedance spectroscopy, using PBS as the electrolyte medium (**Figure 1**). A 3-electrode setup was prepared by screen-printing graphene nanoplatelets formulated in a proprietary ink onto flexible PET substrates,[52] in order to produce

the working and the counter electrodes whereas silver ink served as the reference electrode. CV curves were acquired over a potential range from -0.6 to +0.6 V (scan rate = 50 mV s^{-1}), in order to avoid water electrolysis,[35] in line with previous reports on graphene-based electrodes for brain interfaces.[29,57] Graphene-based electrodes maintained a practically constant current between -0.4 and +0.4 V (**Figure 1a**), which is illustrative of capacitive charge conduction rather than Faradaic redox processes.[29,58] A sharper variation of current between -0.4 and -0.6 V may be attributed to residual oxygen functionalities, which favor proton adsorption and may be partially involved in redox reactions associated with pseudocapacitance.[58,59] This phenomenon was exacerbated upon exposure to radiation from UV to NIR range (λ = 405, 785, 980 nm), evidenced by the enhanced cathodic current around -0.3 V. This observation indicates a reduction process, highlighting the effect of the functional groups on the generation of pseudocapacitance on the graphene surface.[59] This response to light could be attributed to the generation of heat that is dissipated in the graphene lattice after relaxation of photoexcited electrons, supporting charge conduction with additional thermal energy.[60] Considering the broad absorption spectrum of graphene (500 – 2500 nm),[61,62] we reasoned that the electrochemical response of graphene did not depend on light wavelength. In line with previous findings,[41] we obtained similar CV curves across the tested wavelengths, showing an increased cathodal charge storage capacity (CSC) by roughly 65% (p = 0.0310) at an irradiance of 60 mW cm^{-2} (**Figure 1b**).

The effect of light on graphene was further characterized by measuring its impedance (**Figure 1c**). The prepared electrodes revealed comparable characteristics to other graphene-based electrodes suitable for brain interfaces,[27,29,63] such as an area-normalized impedance at 1 kHz of 133.1 ± 22.0 Ω x cm^2 and a CSC of 1.14 ± 0.17 mC cm^{-2}. The Bode plot described a capacitive behavior at low frequencies (< 70 Hz), indicated by the large phase shift between -60° and -75°. At higher frequencies (> 2 kHz), the effects of capacitance decreased as the phase angle approached 0°, hence the solution resistance dictated the measured impedance.[35] Light irradiation (30 mW cm^{-2}) shifted this profile towards lower frequencies (**Figure 1c**), decreasing the cutoff frequency at which the electrode assumes a capacitive behavior (phase angle = -45°) from 180 Hz to approximately 100 Hz.[64] This results in a relaxation time of 1.5 ms, indicating a fast electrical discharge rate.[65] These data suggest that light wavelength might play a role in the capacitive behavior of graphene (**Figure 1d**). While NIR radiation at λ = 980 nm reduced impedance at 100 Hz by 30% (p = 0.0121), a similar response was obtained only at 10 Hz using λ = 780 nm (p = 0.0379), whereas UV light (405 nm) achieved comparable enhancement in conductivity only at 1 Hz (p = 0.0048). Altogether, light exposure enhanced capacitive charge conduction in graphene, particularly in the NIR region. This could be linked to the aforementioned photothermal effect that improves electrical conductivity in graphene.

Hence, we investigated the influence of NIR laser power (λ = 780 nm) in the generation of electric current (**Figure 1e**). The observed variation of current between -0.4 and -0.6 V was more evident at increasing irradiances, suggesting a photothermal reduction of the oxygen functionalities in graphene nanoplatelets. The calculated CSC (**Figure 1f**) and capacitance values (**Figure 1g**) indicated a logarithmic response to laser power (R^2 = 0.9912), producing larger

variations at low irradiance up to 0.3 W cm^{-2}, above which only small incremental increases were observed. Electrode photoresponsivity was also modelled by a logarithmic function (R^2 = 0.9998), with higher laser powers generating less current (**Figure 1h**). This could be attributed to the excess of photoexcited electrons which saturate the energy levels in the conduction band.[47] Overall, our results supported the application of NIR radiation to enhance the electrical conductivity of GBM biointerfaces. However, this may be limited to low laser powers (< 100 mW cm^{-2}) and exposure times (< 5 min) as photothermal effects start to dominate the material's behavior and become detrimental for its biocompatibility (**Figure S1, Supporting Information**).

3.2. Enhancing photoresponse of graphene-based electrodes with UCNPs

In order to improve the performance of these electrodes toward light-responsive biointerfaces, we hypothesized that the incorporation of UCNPs would improve its sensitivity to low-power NIR radiation. First, we prepared a library of UCNPs with different combinations of lanthanides with compatible energy gaps (**Figure 2**),[66] with the aim of optimizing the lanthanide composition leading to the greatest improvement in electrical conductivity upon NIR activation. While high-throughput strategies enable screening all possible combinations,[67] mathematical modelling based on orthogonal Design of Experiments (DoE) can identify which elements in UCNPs are crucial for optimal generation of electric current from graphene nanoplatelets with a minimal number of experiments.

Considering that dopant concentration may affect fluorescence emission due to multiple energy transfer processes between ions,[68] we generated a library of UCNPs with different combinations of sensitizers (Yb, Nd) and activators (Tm, Er, Sm), each set at 3 different molar ratios. Two different sensitizer elements were considered to enable activation of UCNPs at λ = 780 nm or 980 nm. This was motivated by the different response of SH-SY5Y cells cultured on graphene substrates to NIR radiation (100 mW cm^{-2}, 5 min), with λ = 980 nm but not 780 nm apparently inducing cell proliferation (**Figure S1, Supporting Information**). To potentially benefit from this effect, UCNPs can be doped with Yb for activation at λ = 980 nm, which may significantly improve spatial resolution of transcranial activation due to reduced Rayleigh scattering (1/λ^4).[69] Nevertheless, activation at λ = 780 nm enabled by the incorporation of Nd is also attractive owing to reduced light absorption by water, which improves its penetration in biological tissue and avoids overheating.[69,70] These lanthanides were incorporated in NaYF$_4$ or NaGdF$_4$ nanocrystals, since the presence of Gd not only confers paramagnetic features for magnetic resonance imaging but also bridges energy transfer between excited ions, thus improving UCNP fluorescence.[66,71] These UCNPs were then coated with a thin shell layer of optically inert NaYF$_4$ to minimize surface quenching at the interface with water in physiological milieu.[72,73] Using DoE, we reduced all possible 486 combinations (2 nanocrystals x 3^5 dopant combinations) to a library with 18 different candidates (**Figure S2, Supporting Information**). Two additional UCNP formulations (R-04, FR-12) were added as common formulations reported in the literature,[45,54] while a nanocrystal lacking any dopants (FR-13) was used as a negative control, in order to account for any changes in

electrical conductivity to the chemical composition of UCNPs rather than to any thermal effect of NIR radiation. Each of the 21 UCNP formulations was dispersed in 20 μL milliQ water at a fixed concentration of 25 mg mL^{-1} for deposition onto graphene electrodes by drop-casting (0.5 mg).

These graphene-based electrodes were characterized by CV to evaluate the electrochemical response to NIR radiation at λ = 780 nm (**Figure 2a,c**) and/or 980 nm (**Figure 2b,d**), depending on the incorporation of Nd or Yb as sensitizers, respectively. In order to avoid photothermal effects causing cell death (**Figure S1, Supporting Information**), these electrodes were exposed to NIR radiation at a fixed laser power of 30 mW cm^{-2}, which resulted in a high photoresponse (**Figure 1h**). In graphene alone, the application of NIR radiation at λ = 780 nm using these settings could evoke a total current of approximately 187 μA cm^{-2} (**Figure 1h**), which is comparable to relevant electrical stimulation modalities.[35]

Because UCNPs could be partially redispersed in the electrolyte solution, each sample was evaluated by comparing the electrode capacitance in the presence or absence of NIR radiation (**Figure S2, Supporting Information**). This variation in capacitance upon exposure to NIR radiation was compared to the negative control (FR-13). Out of the 20 lanthanide-doped UCNP formulations, A-06 was the best candidate when using NIR radiation at λ = 780 nm (**Figure 2a**), outperforming other UCNP formulations containing Nd (*p* = 0.0422) by increasing capacitance to 2.7-fold (± 0.4) compared to the same electrodes without light activation (p = 0.0038). Using NIR radiation at λ = 980 nm (**Figure 2b**), B-02 was the best hit among UCNP formulations containing Yb (*p* = 0.0154), enhancing capacitance by 106.4 ± 12.3% compared to the same electrodes without light activation (p = 0.0002). The presence of UCNPs resulted in CV curves representative of capacitive charge conduction (**Figure 2c-d**) despite minor changes compared to the original graphene-based electrodes (**Figure 1e**), such as the sharp decrease of the anodic current between -0.6 and -0.2 V. Altogether, these results indicated that although the presence of UCNPs interfered with the aforementioned pseudocapacitance phenomenon upon NIR irradiation, their chemical composition could greatly improve the electrode's capacitive response to light.

In order to understand the influence of lanthanide composition in the capacitance of graphene-UCNP electrodes upon NIR activation, the optimal capacitance values for each UCNP formulation were fitted using a standard least squares regression (**Figure 2e**). The obtained screening model (R^2 = 0.89, *p* = 0.004) identified several statistically significant factors that affected capacitance (**Figure 2f**). Interestingly, all 3 activator elements (Tm, Er, Sm) significantly interacted with each other, with Tm hindering capacitance while Er and Sm augmented it upon NIR activation (**Figure S2, Supporting Information**). These elements are responsible for accumulating energy after photon absorption by the sensitizers, mediating multiple energy transfer processes. The negative interactions of Tm with Er and Sm indicate that energy transfer to Tm may be inefficient and result in energy loss, whereas the positive interaction between Er and Sm may be attributed to the influence of Sm in minimizing low-energy fluorescence emission, leading to enhanced green fluorescence.[67,71] In line with these findings, the identified hits (A-06, B-02) shared a high concentration of Sm (5%) and lacked Tm in their composition (**Figure S2,**

Supporting Information). The sensitizers had a lower impact on the electrical conductivity of graphene, despite the significant interactions of Nd with both Yb and Tm (**Figure 2f**). Finally, the choice of the host nanocrystal played a small role on the generation of capacitance (p = 0.0083), with NaYF$_4$ formulations (identified with letter A) having a poorer performance (negative coefficient) than NaGdF$_4$ (**Figure 2f**). This could be explained by the greater stability of NaGdF$_4$ nanocrystals (identified with letter B) in accommodating larger Sm and Nd ions while minimizing energy loss due to cross-relaxation between neighboring atoms.[71]

Overall, our model highlights that graphene-UCNP electrodes require formulations capable of accumulating photoexcited electrons in the conduction band of UCNPs, leaving holes in their valence band which promote the migration of electrons from graphene.[45,46] This phenomenon generates an electric field which may explain the enhanced cathodic current elicited by UCNPs upon NIR activation (**Figure 2c-d**).

3.3. Covalent conjugation of UCNPs to constitute graphene-UCNP biointerfaces

Our results suggest that graphene-UCNP nanocomposites are promising candidates for light-activatable brain interfaces. Other nanomaterials such as silicon nanowires (SiNW) and black phosphorus (BP) nanosheets have recently achieved promising results in light-mediated stimulation of cells.[74–76] However, while SiNW mediate photothermal and photoelectrochemical effects via Faradaic charge conduction, BP nanosheets stimulated neuronal activity through heat upon NIR activation. Furthermore, these nanomaterials have limited stability in physiological milieu, with oxidative processes driving their biodegradation within 2 weeks.[74,77]

In order to extend their longevity in physiological milieu, we covalently conjugated UCNPs to graphene nanoplatelets (**Figure 3**). This approach was first optimized using UCNPs coated with a thin silica layer (~2 nm) comprised of a mixture of organosilanes bearing primary amine and azide groups.[54] These amines enabled the attachment of UCNPs to graphene nanoplatelets via Michael addition reaction (**Figure 3a**), following the acrylation of graphene (**Figure 3b**). This method was chosen to target already existing defects in the crystal structure of graphene, in order to avoid loss of electrical conductivity. Acrylation was conducted at room temperature using acryloyl chloride, which selectively targets hydroxyl groups without significantly affecting the colloidal stability of graphene in water (**Figure 3b**).[78] Optimal reaction conditions resulted in the introduction of 13.95 ± 0.08 nmol vinyl groups mg^{-1} graphene (**Figure 3b-c**), which decreased by 72% (p = 0.0002) after reaction with the primary amines of silica-coated UCNPs (**Figure 3c**). Quantification of Y by ICP-MS revealed that UCNPs were attached in the composite (107.2 ± 14.6 ng Y µg^{-1} composite), resulting in an estimated conjugation efficiency of 15.6 ± 3.7% (**Figure 3d**).

Covalent immobilization of UCNPs onto graphene nanoplatelets was finally validated by FTIR spectroscopy (**Figure 3e**) and XPS spectroscopy (**Figure 3f**). FTIR spectroscopy revealed characteristic features of graphene nanoplatelets that were maintained throughout their chemical modification and conjugation with UCNPs, including a broad band between 3000 and 3600 cm^{-1} evidencing the presence of hydroxyls and carboxylic acids by O-H stretching vibrations, followed

by small peaks between 2850 and 2925 cm^{-1} which can be ascribed to C-H stretching vibrations of aliphatic carbon atoms, and bands around 1650 and 1560 cm^{-1} corresponding to in-plane C=C stretching vibrations of aromatic carbon partially masked by adsorbed water molecules.[79] Graphene nanoplatelets presented additional features proving the abundance of hydroxyl groups, such as the sharp peak at 1380 cm^{-1} corresponding to O-H bending vibrations of phenols, as well as a band with peaks at 1090 and 1050 cm^{-1} which can be assigned to C-O stretching vibrations.[79] Acrylation selectively targeted the hydroxyl groups of graphene nanoplatelets, resulting in the disappearance of the peak at 1380 cm^{-1} and the emergence of peaks at 950 and 1010 cm^{-1}, corresponding to C-H wagging vibrations of vinyl groups. The presence of UCNPs in graphene-UCNP composites was demonstrated by the detection of fluorine and nitrogen in XPS survey spectra (**Figure 3f**), which could be ascribed to the UCNP nanocrystal and its silica coating, respectively. FTIR spectroscopy (**Figure 3e**) also revealed the emergence of several features attributed to their silica coating, including: i) pronounced peaks around 2850 and 2925 cm^{-1}, owing to the silane alkyl chain of the silane groups; ii) a broad band with peaks at 1030, 1060, and 1090 cm^{-1} which can be assigned to Si-O-Si and C-N bonds;[54] iii) sharp peaks at 800 and 1260 cm^{-1}, corresponding to Si-C bonds. Moreover, the presence of azides could be detected by the small peak at 2100 cm^{-1}, whereas free primary amines could be detected at 1460 cm^{-1} due to hydrogen bonding.[54] Covalent conjugation of UCNPs via Michael addition of primary amines of UCNPs to the vinyl groups of acrylated graphene was demonstrated by the disappearance of the peak at 950 cm^{-1}, alongside the emergence of a band around 3200 cm^{-1}, which was ascribed to N-H stretching vibrations in secondary amines.

Using this strategy, the best UCNP formulations (A-06 and B-02) were attached to graphene nanoplatelets, and the resulting nanocomposites (GU1 and GU2, respectively) were characterized with respect to their size and surface chemistry (**Figure 4**). TEM showed that most silica-coated UCNPs had a diameter between 30 and 50 nm (**Figure 4a-b**) and comparable ζ-potential values (**Figure S3, Supporting Information**), owing to the presence of positively charged amines. High-resolution XPS spectra allowed the detection of several lanthanides in UCNPs (**Figure S3, Supporting Information**) and further demonstrated that silica coating was similar to both UCNP formulations (**Figure S4, Supporting Information**). While acrylation did not affect the size of graphene nanoplatelets, the resulting nanocomposites after conjugation with UCNPs were slightly larger (**Figure 4c-d** and **Figure S5, Supporting Information**), with average lateral dimensions between 1 and 2 μm (**Figure 4d**). This could be attributed to the more neutral ζ-potential around -11 mV (**Figure 4e**), owing to the presence of positively charged UCNPs counteracting the negative surface charge of graphene nanoplatelets. Nevertheless, these composites remained sufficiently stable in colloidal dispersion for deposition by spray coating. XPS survey spectra demonstrated the high chemical purity of graphene nanoplatelets (96.1 ± 0.1%), resulting in a C/O ratio of 2.65 (**Table S1, Supporting Information**). Acrylation resulted in a decreased oxygen abundance, which could be ascribed to the selective reaction towards hydroxyl groups, characterized by the sharp decrease of detected C-O bonds (**Figure S5, Supporting Information** and **Table S2, Supporting Information**). The nanocomposites

maintained a low oxygen content compared to the original graphene nanoplatelets (**Figure 4f**), which was characterized by a greater contribution of carboxyl groups (**Figure 4g** and **Tables S2-S3, Supporting Information**) possibly due to the constitution of ester bonds between graphene and UCNPs (**Figure 3a**).

Overall, we demonstrated the successful covalent immobilization of UCNPs to graphene nanoplatelets with suitable physicochemical properties for screen-printing cell substrates.

3.4. *In vitro* activity of graphene-UCNP biointerfaces

Finally, we investigated whether the prepared graphene-UCNP nanocomposites could modulate brain cell proliferation and differentiation upon exposure to NIR radiation. While GBMs have been employed as electroactive substrates for neuronal cell culture,[32–34] several studies have reported enhanced neuronal differentiation of neural stem and progenitor cells.[80–82] This effect has been attributed to the raise in intracellular calcium levels leading to the production of neurotrophic factors via FAK and p38 MAPK signaling.[34,80,81] Akhavan *et al.* investigated the impact of light stimulation in the differentiation of human neural stem cells cultured on graphene-based substrates.[83,84] While the authors could mimic the effects of electrical stimulation through the generation of photoelectrons, the heat generated by light exposure (especially NIR radiation) could impede the application of these GBMs alone *in vivo*. Hence, we hypothesized that the use of low-power NIR radiation, enabled by the conjugation of UCNPs to graphene nanoplatelets, could promote cell differentiation without significant cytotoxicity.

To evaluate the biocompatibility and capability of using NIR radiation to stimulate cell activity, we used the human SH-SY5Y neuroblastoma cell line which serves as a neural progenitor cell model capable of undergoing differentiation to neuronal-like cells presenting characteristic features of cholinergic, adrenergic, or dopaminergic neurons.[56,85] Its versatility has been employed in the development of *in vitro* cell models for neurodegenerative diseases including AD and PD.[86,87] First, toxicological dose-response relationships were established after incubating SH-SY5Y cells with each individual component (in suspension) involved in the conjugation of graphene with UCNPs. The assay was done in the absence of serum proteins for the first 4 h of treatment, in order to determine the potential risks associated with exposure to the resulting graphene-based formulations, followed by 20 h of incubation with medium supplemented with serum.[88,89] Cytotoxicity was assessed 24 h after exposure by propidium iodide staining (**Figure 5a**). Graphene nanoplatelets showed a dose-dependent increase of dead cells that was more pronounced in their acrylated counterparts (20 µg mL^{-1}, p = 0.0240) compared to the original material (50 µg mL^{-1}, p < 0.0001). A similar trend was observed with respect to metabolic activity, which decreased as the nanoplatelet dose increased (**Figure S6, Supporting Information**). In contrast, the conjugation of UCNPs to graphene rescued the material biocompatibility, which can be ascribed to a negligible amount of free vinyl groups (**Figure 3c**). Although cytotoxicity of GBMs to SH-SY5Y cells has been linked to mitochondrial dysfunction via the generation of reactive oxygen species (ROS),[90] no significant oxidative stress was observed after treatment with

16

graphene-UCNP composites (**Figure S6, Supporting Information**). These results supported further investigations on the application of NIR radiation on cells cultured on planar graphene-UCNP substrates, which were prepared by spray coating onto PET films.

The effect of NIR radiation on cell proliferation was initially evaluated by cell cycle analysis performed 72 h after incubation on planar graphene-based substrates (**Figure 5b-c** and **Figure S7, Supporting Information**). While both graphene-UCNP formulations (GU1, GU2) increased the number of mitotic cells in G2/M phase (p = 0.0127), GU2 had a more profound effect than GU1 in shifting cell cycle (**Figure 5c**) by also increasing the number of cells in S phase (p = 0.0026). NIR radiation at λ = 980 nm (100 mW cm^{-2}, 5 min) further increased the number of SH-SY5Y cells in S (p = 0.0146) and G2/M phases (p = 0.0041) on GU2 films (**Figure 5d**). However, cells cultured on GU1 substrates did not suffer any changes in cell cycle after exposure to NIR radiation at λ = 780 nm. These results could be ascribed to the influence of NIR radiation at λ = 980 nm on cell proliferation (**Figure S1, Supporting Information**), which also increased cell density of SH-SY5Y cells cultured on graphene or PET films (**Figure S6, Supporting Information**). This was validated by immunocytochemical analysis of proliferation marker Ki67 (**Figure 5e**), revealing a stronger expression in cells cultured on GU2 compared to graphene and GU1 (**Figure 5f** and **Figure S8, Supporting Information**). Interestingly, cells cultured on GU2 substrates maintained their expression of Ki67 after exposure to NIR radiation at λ = 980 nm (p = 0.6895), whereas NIR radiation at λ = 780 nm decreased Ki67 expression of cells cultured on GU1 substrates (p < 0.0001).

Finally, the effect of NIR exposure (100 mW cm^{-2}, 5 min) on the differentiation of SH-SY5Y cells cultured on graphene-UCNP nanocomposites was investigated by immunocytochemical analysis of glial (GFAP) and neuronal (DCX) differentiation markers (**Figure 6a-d**).[91] In line with their phenotype resembling neural progenitor cells, SH-SY5Y cells cultured on graphene-based substrates expressed both GFAP and DCX, which remained unaltered after exposure to NIR radiation at λ = 780 nm (**Figure S8, Supporting Information**). Conversely, NIR radiation at λ = 980 nm seemed to induce neuronal differentiation in these cells, indicated by the increased DCX expression (p = 0.0166), accompanied by the upregulation of Ki67 (p = 0.0199) which supported previous observations of increased cell proliferation. Compared to graphene, both GU1 and GU2 substrates upregulated the expression of Ki67 (p = 0.0013) and DCX (p = 0.0018). Nevertheless, only GU2 was capable of increasing the expression of GFAP (p = 0.0011), which decreased (p = 0.0008) after exposure to NIR radiation at λ = 980 nm (**Figure 6b**). Similarly, NIR radiation decreased DCX expression (p < 0.0001) in cells on GU2 substrates (**Figure 6d**). In contrast, GFAP expression was unaffected by NIR radiation at λ = 780 nm, whereas DCX expression decreased (p = 0.0008) in cells cultured on GU1 substrates (**Figure S8, Supporting Information**). Considering that these cells were not affected by NIR radiation with respect to their cell cycle (**Figure 5d**), the effect of NIR radiation at λ = 780 nm on the activity of cells cultured on GU1 substrates may actually be detrimental due to high-energy photoexcited electrons.[84]

Overall, our results suggest that both the substrate and the NIR wavelength used to activate SH-SY5Y cells can affect their proliferation and differentiation. These effects are unlikely

related to the electrochemical behavior of the substrates under NIR irradiation, considering the similar profiles of graphene alone (**Figure 1a**) or with the respective UCNPs (**Figure 2c-d**). While the exact molecular mechanisms are still unknown, there is growing evidence that several materials employed as substrates can influence proliferation and differentiation of neural stem and progenitor cells via ROS generation.[92,93] We and others have previously shown that increasing ROS levels using nanomaterials and/or light promotes differentiation of neural stem cells and SH-SY5Y cells.[91,94] In contrast, a low redox state characterized by a lower production of ROS may favor proliferation of less differentiated cells.[93] Therefore, ROS generation in SH-SY5Y cells exposed to GU1 or GU2 nanocomposites (in suspension) was quantified in the presence or absence of NIR radiation (**Figure 6e**). Cells exposed to the nanocomposites had a lower baseline ROS production compared to untreated cells, even though it was only statistically significant for GU1 (p = 0.0489). Thus, these results may explain the higher cell proliferation after culture in planar GU1 or GU2 nanocomposites compared to planar graphene substrates (**Figure 5b-f**). Although cells treated with either GU1 or GU2 maintained their baseline ROS production levels after exposure to NIR radiation at λ = 980 nm, they were significantly lower than those in irradiated cells unexposed to NPs (p = 0.0052). Interestingly, NIR radiation at λ = 780 nm increased ROS generation in cells treated with GU1 nanoparticles compared to cells unexposed to radiation (p = 0.0404), whereas cells treated with GU2 exhibited lower ROS production than irradiated cells unexposed to NPs (p = 0.0006). These results indicate that cells treated with GU2 maintain a low redox state irrespective of exposure to NIR radiation, which may explain the reduced expression of differentiation markers GFAP and DCX of cells cultured on GU2 substrates (**Figure 6a-d**). Although cells cultured on GU1 substrates exhibited similar reduction in the expression of differentiation markers, this was accompanied by a lower expression of Ki67 (**Figure S8, Supporting Information**). This indicated that exposure to NIR radiation at λ = 780 nm impaired the proliferation of cells cultured on GU1 substrates, which could be attributed to the increased ROS production (**Figure 6e**). Oxidative stress could be induced by photothermal effects associated with exposure of GBMs to NIR radiation. Further experimental efforts are warranted in the near future to elucidate this potential mechanism. In addition, further work is needed in the near future to elucidate whether other factors than ROS production (e.g. material properties) may contribute to modulating the expression of cell differentiation markers.

Our findings contrast with previous reports on the use of graphene-based substrates to culture SH-SY5Y cells, which promote neuronal differentiation.[80,82] This could be explained by the application of a short stimulation regime (5 min) in cells experiencing an earlier stage of differentiation, which are more sensitive to calcium influx induced by membrane depolarization.[95] NIR activation enhanced cathodic charge injection from graphene-UCNP electrodes (**Figure 2a-d**), resulting in the accumulation of electrons which decrease cell membrane polarization. While cell differentiation has been achieved using long stimulation protocols (> 6 h),[34] the application of short depolarization stimuli was shown to promote the proliferation of SH-SY5Y cells by modulating the cell cycle toward the S phase,[96] in agreement with our observations (**Figure 5b-d**). We anticipate that longer stimulation periods enabled by the application of light pulses will

mimic the effects of prolonged membrane depolarization in neural progenitor cells, particularly their differentiation towards dopaminergic neurons.[97] Altogether, our results suggest that NIR radiation at λ = 980 nm may be used to target neural progenitor cells in neurogenic niches to promote their proliferation.

4.   Conclusion

In summary, we have demonstrated that graphene nanoplatelets are capable of eliciting capacitive charge conduction upon exposure to NIR radiation. We reported an innovative platform of graphene nanoplatelets conjugated with UCNPs which increases their sensitivity to NIR radiation and enables optical cell stimulation. The present platform differentiates from other systems developed for NIR activation of neurons with the application of biocompatible nanomaterials that are stable in physiological milieu. The versatility enabled by the formulation reported here might find application in the treatment of neurodegenerative diseases including AD and other disorders caused by brain injury (e.g., stroke), where tissue regeneration is impaired by excessive ROS production.[98–100] Our results suggest the application of NIR radiation at λ = 980 nm in cells exposed to GU2 nanocomposites may decrease ROS production and support the proliferation of neural progenitor and stem cells, followed by their differentiation to neurons in the absence of NIR radiation. Further research is warranted to understand cell response to different stimulation protocols, including the variation of specific parameters such as frequency and the time window in which it is applied, in order to optimize the settings for *in vivo* stimulation. These electrodes could also be complemented with the targeted delivery of bioactive molecules to confer long-term control over cell proliferation and differentiation in specific regions with precise temporal resolution.[91,101,102]

The spatiotemporal resolution of NIR radiation enables selective targeting of cortical regions to promote neurogenesis and remodel neuronal circuitry. This strategy can become even more precise by rendering graphene-UCNP electrodes sensitive to biochemical cues through the specific detection of neurotransmitters (e.g. dopamine), using molecularly imprinted polymers that can be synthesized after conjugation with the free azide groups of UCNPs.[103] Neurotransmitters can act as electron acceptors and capture photoexcited electrons in UCNPs,[104] thus reducing the generated electric signal in regions where electrical stimulation is not desirable. Other brain structures susceptible to neurodegeneration with ageing and pathological processes such as PD may warrant further formulation development to increase the electrode's sensitivity, in order to overcome the limited penetration depth of NIR radiation in the human brain. This can be achieved by rational design of the UCNPs employed in the composite. While DoE showed a synergistic effect of Er and Sm in enhancing the generation of electric current, UCNPs can be further engineered with different crystal phases and sizes by adjusting reaction temperature and time, as well as the nature and concentration of surfactants.[105] Furthermore, the $NaYF_4$ shell could become optically active by incorporating different lanthanides with the aim of increasing the number of energy transitions in the nanocrystal.

Author contributions

AFR, TS and LF devised the project and supervised the work. AFR performed nanomaterial synthesis and characterization, and *in vitro* biological studies. APMT performed electrochemical characterization of graphene-based electrodes, under the supervision of GS. SS performed immunofluorescence analysis of stimulated cells. RS and BF produced graphene nanoplatelets and screen-printed electrodes. The manuscript was written by AFR and LF, with contribution from all authors. All authors approved its final version before submission.

Conflicts of interest

The authors declare no competing financial interest.

Acknowledgments

Figure Legends

Figure 1. Electrochemical characterization of screen-printed graphene electrodes. (a) Representative cyclic voltammetry (CV) curves of graphene electrodes exposed to light at different wavelengths (405, 780, 980 nm) using a fixed laser power (60 mW cm^{-2}). **(b)** Cathodic charge storage capacity (CSC) was calculated by integration of the negative sweep (area below the dashed line in the CV curve. Results are expressed as mean ± SEM (n = 3). One-way ANOVA with *post hoc* Tukey's multiple comparisons test was performed: **(*)**, $p < 0.05$. **(c)** Representative Bode plots of graphene electrodes exposed to light at a laser power of 60 mW cm^{-2}. Dashed line corresponds to a -45º phase angle, in order to determine at which frequency the electrode becomes capacitive. **(d)** Variation in impedance induced by light was compared at different frequencies. Results are expressed as mean ± SEM (n = 3). Two-way ANOVA with *post hoc* Dunnett's multiple comparisons test against non-irradiated electrodes was performed: **(*)**, $p < 0.05$; **(**)**, $p < 0.01$. **(e)** Representative CV curves of graphene electrodes exposed to NIR radiation at λ = 780 nm, using different irradiances. **(f)** CSC and **(g)** capacitance increased with laser power following a logarithmic function (**g**, inset). **(h)** Electrode photosensitivity to NIR radiation at λ = 780 nm was also modelled by a logarithmic function.

Figure 2. Effect of UCNP composition on the electrical conductivity of graphene electrodes after NIR activation. UCNPs were drop-casted onto graphene electrodes and their electrochemical response to NIR radiation (30 mW cm^{-2}) was measured by CV. Only one candidate was identified after irradiation at **(a)** λ = 780 nm and **(b)** λ = 980 nm, showing a statistically significant increase in capacitance following NIR exposure against pure NaYF$_4$ nanocrystals lacking lanthanide dopants (dashed lines). Results are expressed as mean ± SEM (n = 2-3). For each wavelength, one-way ANOVA with *post hoc* Tukey's multiple comparisons test was performed: **(*)**, $p < 0.05$. **(c)** Representative CV curves of lead candidates with (red) or without (black) exposure to NIR radiation at λ = 780 nm or **(d)** λ = 980 nm. **(e)** The highest variation in capacitance obtained with NIR radiation (λ = 780 or 980 nm) was correlated with UCNP composition by multivariate analysis. **(f)** List of parameters used in predictive model after eliminating statistically insignificant ($p > 0.05$) parameters one-by-one. Insignificant parameters in the model were maintained due to significant first-order interactions between lanthanides.

Figure 3. Conjugation of graphene nanoplatelets with UCNPs. (a) Graphene-UCNP composites were produced via Michael addition, following acrylation of graphene nanoplatelets. **(b)** Quantification of vinyl groups introduced by acrylation was performed using a fluorescent probe targeting these moieties via thiol-Michael click reaction. Optimization of reaction conditions aimed to maximize the abundance of vinyl groups without impacting the colloidal stability of acrylated graphene. Optimal condition was highlighted with a green bar. Results are expressed as mean ± SEM (n = 3). Two-way ANOVA with *post hoc* Dunnett's multiple comparisons test against non-irradiated electrodes was performed: **(**)**, $p < 0.01$. **(c)** Quantification of vinyl and primary amines in acrylated graphene (GA) and the resulting graphene-UCNP composites (GU)

was performed to optimize the immobilization of silane-coated UCNPs (estimated by amine content). The introduced vinyl groups after acrylation were reactive towards the primary amines of UCNP (~63 groups per UCNP). The selected dose of 80 µmol acryloyl chloride mg^{-1} graphene underwent a significant reduction in vinyl content and exhibited a greater content of primary amines, suggesting the efficient conjugation of UCNPs. Vinyl content was assessed by two-way ANOVA with *post hoc* Sidak's multiple comparisons test: **(***)**, $p < 0.001$. **(d)** Quantification of yttrium (Y) by ICP-MS in graphene nanoplatelets before (G) and after immobilization of UCNPs (GU). Results are expressed as mean ± SEM (n = 2-3). Two-tailed unpaired t test was performed: **(*)**, $p < 0.05$**.** The yield of conjugation of UCNPs to graphene nanoplatelets was represented by the estimated amount of UCNPs in each sample, which was derived by dividing the obtained amount of Y per mass of lyophilized sample by the value obtained for pure UCNPs (773.1 ± 16.5 ng Y µg^{-1} UCNP). **(e)** FTIR spectra of graphene nanoplatelets (G), acrylated graphene (GA), and graphene-UCNP (GU) describe the modifications in surface chemistry of graphene throughout the reaction steps. Dashed lines at 1650 cm^{-1} and 1380 cm^{-1} highlight the contributions of aromatic carbon and phenol groups, respectively, demonstrating the selectivity of the acrylation reaction toward hydroxyl groups. The reaction of vinyl groups with primary amines of UCNPs was demonstrated by the disappearance of the peak at 950 cm^{-1} alongside the emergence of a shoulder around 3200 cm^{-1}, indicative of secondary amines. **(f)** XPS survey spectra of GBMs highlighting the changes in carbon and oxygen content, as well as the introduction of nitrogen and fluorine from UCNPs.

Figure 4. Characterization of graphene-UCNP nanocomposites. (a) Representative TEM image of B-02 UCNPs. Scale bar = 100 nm. **(b)** Size distributions of lead UCNP formulations A-06 and B-02 were fitted to a Gaussian distribution. **(c)** Representative TEM image of GU2 illustrates the attachment of small UCNP clusters (highlighted with yellow arrows), following the conjugation of B-02 UCNPs to graphene nanoplatelets. Scale bar = 1 µm. **(d)** Average particle size was determined by manually measuring the longest Feret diameter of >100 NPs. **(e)** Surface charge of GBMs determined by ζ-potential. Results are expressed as mean ± SEM (n = 5). In **(d)** and **(e)**, one-way ANOVA with Tukey's multiple comparisons test was performed: **(**)**, $p < 0.01$; **(****)**, $p < 0.0001$. **(f)** High-resolution C1s and **(g)** O1s spectra of graphene nanoplatelets before (G) and after conjugation with UCNPs (GU1 and GU2).

Figure 5. Impact of graphene-UCNP nanocomposites on the proliferation of SH-SY5Y neuroblastoma cells. (a) Viability of SH-SY5Y cells was assessed 24 h after treatment with GBMs by determining the percentage of PI-stained cells using high-content imaging. Cells were treated with GBMs and UCNPs over a range of concentrations (5 – 200 µg mL^{-1}). DMSO (10% v/v) was used as a positive control. Results are expressed as mean ± SEM (n = 3). Two-way ANOVA with *post hoc* Dunnett's multiple comparisons test against the untreated control was performed: **(*),** $p < 0.05$; **(***)**, $p < 0.001$; **(****)**, $p < 0.0001$. **(b)** Effect of GBM substrate and NIR radiation (100 mW cm^{-2}, 5 min) on cell cycle of PI-stained SH-SY5Y cells was determined by flow cytometry. **(c)** Conjugation of UCNPs with graphene nanoplatelets significantly increased the

number of cells in the G2/M of the cell cycle and decreased the number of cells in G0/G1. Results are expressed as mean ± SEM (n = 3). Two-way ANOVA with *post hoc* Tukey's multiple comparisons test was performed: **(*)**, $p < 0.05$; **(**)**, $p < 0.01$; **(***)**, $p < 0.001$; **(****)**, $p < 0.0001$. **(d)** Effect of NIR radiation in each graphene-UCNP nanocomposite was evaluated by comparing cell populations in G0/G1, S, and G2/M phases of the cell cycle. Results are expressed as mean ± SEM (n = 3). One-way ANOVA with *post hoc* Tukey's multiple comparisons test was performed: **(*)**, $p < 0.05$; **(**)**, $p < 0.01$. **(e)** Representative immunofluorescence images of Ki67 expression in SH-SY5Y cells cultured on graphene-based substrates with or without exposure to NIR radiation at $\lambda = 980$ nm (100 mW cm^{-2}, 5 min). Scale bars = 10 μm. **(f)** While NIR activation at $\lambda = 980$ nm increased the expression of Ki67 in cells cultured on graphene substrates (G), it was unaltered in cells cultured on graphene-UCNP substrates (GU2). Results are expressed as mean ± SEM (n = 3-4). Two-way ANOVA with *post hoc* Sidak's multiple comparisons test was performed: **(*)**, $p < 0.05$; **(**)**, $p < 0.01$.

Figure 6. Impact of graphene-UCNP nanocomposites on the differentiation of SH-SY5Y neuroblastoma cells. SH-SY5Y cells cultured on graphene-based substrates and exposed to NIR radiation at $\lambda = 980$ nm (100 mW cm^{-2}, 5 min). **(a)** Representative immunofluorescence images of GFAP (yellow) and **(b)** quantification of GFAP expression. **(c)** Representative immunofluorescence images of DCX (green) and **(d)** quantification of DCX expression. While NIR activation at $\lambda = 980$ nm increased the expression of GFAP and DCX and Ki67 in cells cultured on graphene substrates (G), the expression of GFAP and DCX significantly decreased in cells cultured on graphene-UCNP substrates (GU2). In **(a)** and **(c)**, scale bars = 10 μm. In **(b)** and **(d)**, results are expressed as mean ± SEM (n = 3-4). Two-way ANOVA with *post hoc* Sidak's multiple comparisons test was performed: **(**)**, $p < 0.01$; **(***)**, $p < 0.001$; **(****)**, $p < 0.0001$. **(e)** Intracellular ROS production in SH-5YSY cells was measured 4 h after treatment with GU1 or GU2 in suspension (100 μg mL^{-1}), followed by exposure to NIR radiation at $\lambda = 780$ nm or $\lambda = 980$ nm (100 mW cm^{-2}) for 5 min. Results are expressed as mean ± SEM (n = 3). Two-way ANOVA with *post hoc* Tukey's multiple comparisons test was performed: **(*)**, $p < 0.05$; **(**)**, $p < 0.01$; **(***)**, $p < 0.001$; **(****)**, $p < 0.0001$.

References

1   K. M. Tye, *Neuron*, 2014, **83**, 1259–1261.

2   J. K. Krauss, N. Lipsman, T. Aziz, A. Boutet, P. Brown, J. W. Chang, B. Davidson, W. M. Grill, M. I. Hariz, A. Horn, M. Schulder, A. Mammis, P. A. Tass, J. Volkmann and A. M. Lozano, *Nat. Rev. Neurol.*, 2021, **17**, 75–87.

3   C. Buhmann, T. Huckhagel, K. Engel, A. Gulberti, U. Hidding, M. Poetter-Nerger, I. Goerendt, P. Ludewig, H. Braass, C. U. Choe, K. Krajewski, C. Oehlwein, K. Mittmann, A. K. Engel, C. Gerloff, M. Westphal, J. A. Köppen, C. K. E. Moll and W. Hamel, *PLoS One*, 2017, **12**, e0178984.

4   M. I. Hariz, S. Rehncrona, N. P. Quinn, J. D. Speelman and C. Wensing, *Mov. Disord.*, 2008, **23**, 416–421.

5   A. P. Burdick, H. H. Fernandez, M. S. Okun, Y. Y. Chi, C. Jacobson and K. D. Foote, *Neurosurg. Focus*, 2010, **29**, E4.

6   S. M. Won, E. Song, J. T. Reeder and J. A. Rogers, *Cell*, 2020, **181**, 115–135.

7   J. A. Frank, M. J. Antonini and P. Anikeeva, *Nat. Biotechnol.*, 2019, **37**, 1013–1023.

8   G. Hong and C. M. Lieber, *Nat. Rev. Neurosci.*, 2019, **20**, 330–345.

9   S. Miocinovic, S. Somayajula, S. Chitnis and J. L. Vitek, *JAMA Neurol.*, 2013, **70**, 163–171.

10   O. A. Shemesh, D. Tanese, V. Zampini, C. Linghu, K. Piatkevich, E. Ronzitti, E. Papagiakoumou, E. S. Boyden and V. Emiliani, *Nat. Neurosci.*, 2017, **20**, 1796–1806.

11   J. Delbeke, L. Hoffman, K. Mols, D. Braeken and D. Prodanov, *Front. Neurosci.*, 2017, **11**, 663.

12   S. B. Gonçalves, J. F. Ribeiro, A. F. Silva, R. M. Costa and J. H. Correia, *J. Neural Eng.*, 2017, **14**, 041001.

13   J. Zhang, Y. He, S. Liang, X. Liao, T. Li, Z. Qiao, C. Chang, H. Jia and X. Chen, *Nat. Commun.*, 2021, **12**, 2730.

14   R. Chen, F. Gore, Q. A. Nguyen, C. Ramakrishnan, S. Patel, S. H. Kim, M. Raffiee, Y. S. Kim, B. Hsueh, E. Krook-Magnusson, I. Soltesz and K. Deisseroth, *Nat. Biotechnol.*, 2021, **39**, 161–164.

15   S. Chen, A. Z. Weitemier, X. Zeng, L. He, X. Wang, Y. Tao, A. J. Y. Huang, Y. Hashimotodani, M. Kano, H. Iwasaki, L. K. Parajuli, S. Okabe, D. B. Loong Teh, A. H. All, I. Tsutsui-Kimura, K. F. Tanaka, X. Liu and T. J. McHugh, *Science (80-.).*, 2018, **359**, 679–684.

16   R. Chen, G. Romero, M. G. Christiansen, A. Mohr and P. Anikeeva, *Science (80-.).*, 2015, **347**, 1477–1480.

17   A. Fomenko, C. Neudorfer, R. F. Dallapiazza, S. K. Kalia and A. M. Lozano, *Brain Stimul.*, 2018, **11**, 1209–1217.

18   P. Feyen, E. Colombo, D. Endeman, M. Nova, L. Laudato, N. Martino, M. R. Antognazza, G. Lanzani, F. Benfenati and D. Ghezzi, *Sci. Rep.*, 2016, **6**, 22718.

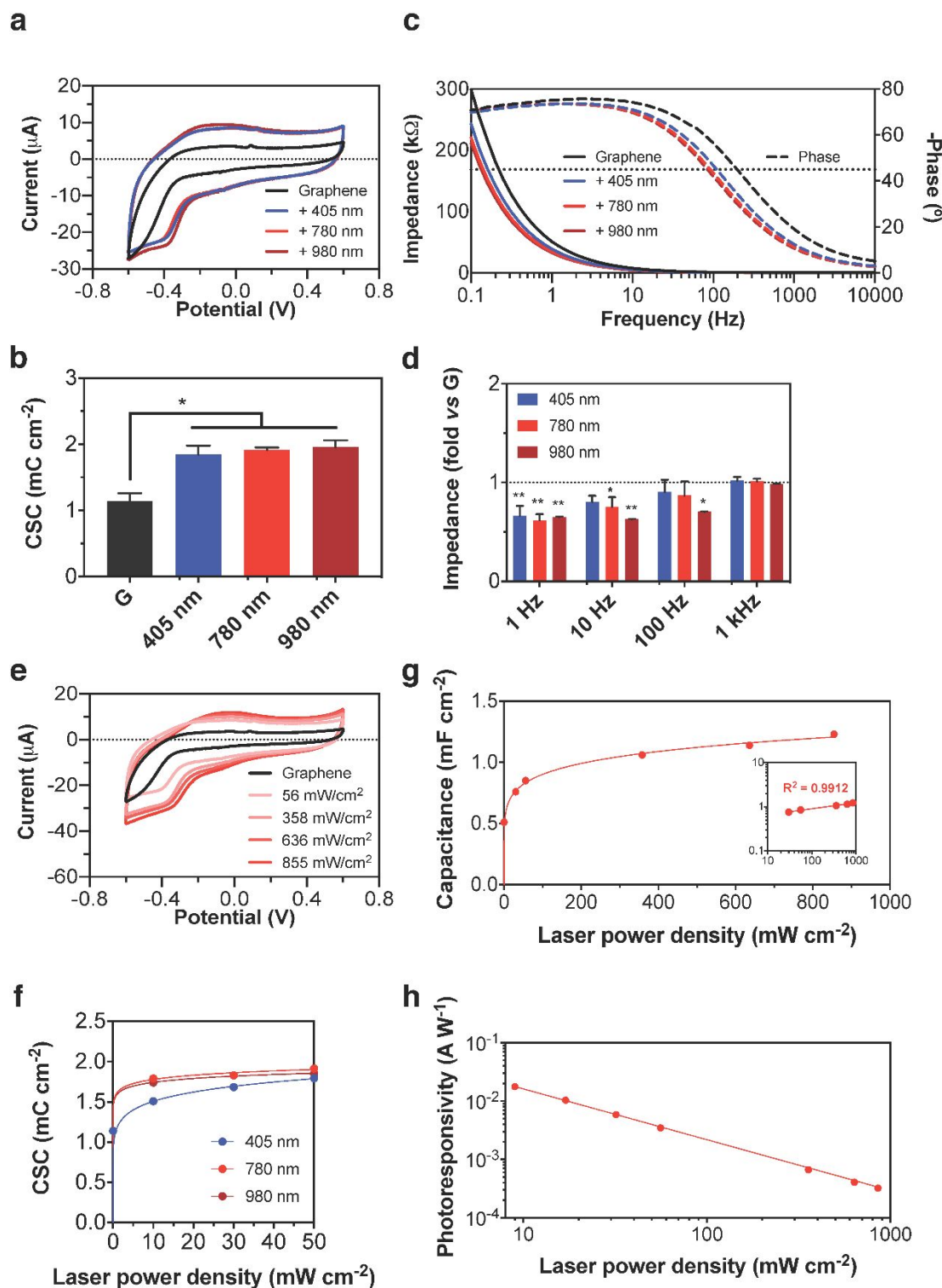19   X. Liu, Z. Qiao, Y. Chai, Z. Zhu, K. Wu, W. Ji, D. Li, Y. Xiao, L. Mao, C. Chang, Q. Wen,

B. Song and Y. Shu, *Proc. Natl. Acad. Sci.*, 2021, **118**, e2015685118.

20   J. Yong, K. Needham, W. G. A. Brown, B. A. Nayagam, S. L. Mcarthur, A. Yu and P. R. Stoddart, *Adv. Healthc. Mater.*, 2014, **3**, 1862–1868.

21   M. Shapiro, K. Homma and S. Villarreal, *Nat. Commun.*, 2012, **3**, 736.

22   K. Kostarelos, M. Vincent, C. Hebert and J. A. Garrido, *Adv. Mater.*, 2017, **29**, 1700909.

23   S. M. Wellman, J. R. Eles, K. A. Ludwig, J. P. Seymour, N. J. Michelson, W. E. McFadden, A. L. Vazquez and T. D. Y. Kozai, *Adv. Funct. Mater.*, 2018, **28**, 1701269.

24   F. Vitale, S. R. Summerson, B. Aazhang, C. Kemere and M. Pasquali, *ACS Nano*, 2015, **9**, 4465–4474.

25   J. Zhang, X. Liu, W. Xu, W. Luo, M. Li, F. Chu, L. Xu, A. Cao, J. Guan, S. Tang and X. Duan, *Nano Lett.*, 2018, **18**, 2903–2911.

26   D. W. Park, A. A. Schendel, S. Mikael, S. K. Brodnick, T. J. Richner, J. P. Ness, M. R. Hayat, F. Atry, S. T. Frye, R. Pashaie, S. Thongpang, Z. Ma and J. C. Williams, *Nat. Commun.*, 2014, **5**, 5258.

27   D. W. Park, J. P. Ness, S. K. Brodnick, C. Esquibel, J. Novello, F. Atry, D. H. Baek, H. Kim, J. Bong, K. I. Swanson, A. J. Suminski, K. J. Otto, R. Pashaie, J. C. Williams and Z. Ma, *ACS Nano*, 2018, **12**, 148–157.

28   S. Zhao, X. Liu, Z. Xu, H. Ren, B. Deng, M. Tang, L. Lu, X. Fu, H. Peng, Z. Liu and X. Duan, *Nano Lett.*, 2016, **16**, 7731–7738.

29   S. Zhao, G. Li, C. Tong, W. Chen, P. Wang, J. Dai, X. Fu, Z. Xu, X. Liu, L. Lu, Z. Liang and X. Duan, *Nat. Commun.*, 2020, **11**, 1788.

30   B. Fadeel, C. Bussy, S. Merino, E. Vázquez, E. Flahaut, F. Mouchet, L. Evariste, L. Gauthier, A. J. Koivisto, U. Vogel, C. Martín, L. G. Delogu, T. Buerki-Thurnherr, P. Wick, D. Beloin-Saint-Pierre, R. Hischier, M. Pelin, F. C. Carniel, M. Tretiach, F. Cesca, F. Benfenati, D. Scaini, L. Ballerini, K. Kostarelos, M. Prato and A. Bianco, *ACS Nano*, 2018, **12**, 10582–10620.

31   A. F. Rodrigues, L. Newman, D. A. Jasim, I. A. Vacchi, C. Ménard-Moyon, L. E. Crica, A. Bianco, K. Kostarelos and C. Bussy, *Arch. Toxicol.*, 2018, **92**, 3359–3379.

32   N. P. Pampaloni, M. Lottner, M. Giugliano, A. Matruglio, F. D'Amico, M. Prato, J. A. Garrido, L. Ballerini and D. Scaini, *Nat. Nanotechnol.*, 2018, **13**, 755–764.

33   A. Fabbro, D. Scaini, V. León, E. Vázquez, G. Cellot, G. Privitera, L. Lombardi, F. Torrisi, F. Tomarchio, F. Bonaccorso, S. Bosi, A. C. Ferrari, L. Ballerini and M. Prato, *ACS Nano*, 2016, **10**, 615–623.

34   Z. Zhang, L. H. Klausen, M. Chen and M. Dong, *Small*, 2018, **14**, 1801983.

35   S. F. Cogan, *Annu. Rev. Biomed. Eng.*, 2008, **10**, 275–309.

36   S. W. Park, J. Kim, M. Kang, W. Lee, B. S. Park, H. Kim, S. Y. Choi, S. Yang, J. H. Ahn and S. Yang, *Small*, 2018, **14**, 1801732.

37   C. Hébert, E. Masvidal-Codina, A. Suarez-Perez, A. B. Calia, G. Piret, R. Garcia-Cortadella, X. Illa, E. Del Corro Garcia, J. M. De la Cruz Sanchez, D. V. Casals, E. Prats-Alfonso, J. Bousquet, P. Godignon, B. Yvert, R. Villa, M. V. Sanchez-Vives, A.

Guimerà-Brunet and J. A. Garrido, *Adv. Funct. Mater.*, 2018, **28**, 1703976.

38   E. Masvidal-Codina, X. Illa, M. Dasilva, A. B. Calia, T. Dragojević, E. E. Vidal-Rosas, E. Prats-Alfonso, J. Martínez-Aguilar, J. M. De la Cruz, R. Garcia-Cortadella, P. Godignon, G. Rius, A. Camassa, E. Del Corro, J. Bousquet, C. Hébert, T. Durduran, R. Villa, M. V. Sanchez-Vives, J. A. Garrido and A. Guimerà-Brunet, *Nat. Mater.*, 2019, **18**, 280–288.

39   W. Wei and X. Wang, *Materials (Basel).*, 2021, **14**, 6170.

40   Y. Lu, X. Liu and D. Kuzum, *Curr. Opin. Biomed. Eng.*, 2018, **6**, 138–147.

41   A. Savchenko, V. Cherkas, C. Liu, G. B. Braun, A. Kleschevnikov, Y. I. Miller and E. Molokanova, *Sci. Adv.*, 2018, **4**, eaat0351.

42   X. Lin, X. Chen, W. Zhang, T. Sun, P. Fang, Q. Liao, X. Chen, J. He, M. Liu, F. Wang and P. Shi, *Nano Lett.*, 2018, **18**, 948–956.

43   X. Lin, Y. Wang, X. Chen, R. Yang, Z. Wang, J. Feng, H. Wang, K. W. C. Lai, J. He, F. Wang and P. Shi, *Adv. Healthc. Mater.*, 2017, **6**, 1700446.

44   B. Zhou, B. Shi, D. Jin and X. Liu, *Nat. Nanotechnol.*, 2015, **10**, 924–936.

45   M. K. Thakur, A. Gupta, M. Y. Fakhri, R. S. Chen, C. T. Wu, K. H. Lin and S. Chattopadhyay, *Nanoscale*, 2019, **11**, 9716–9725.

46   M. Kataria, K. Yadav, G. Haider, Y. M. Liao, Y. R. Liou, S. Y. Cai, H. I. Lin, Y. H. Chen, C. R. Paul Inbaraj, K. P. Bera, H. M. Lee, Y. T. Chen, W. H. Wang and Y. F. Chen, *ACS Photonics*, 2018, **5**, 2336–2347.

47   M. Kataria, K. Yadav, S. Y. Cai, Y. M. Liao, H. I. Lin, T. L. Shen, Y. H. Chen, Y. T. Chen, W. H. Wang and Y. F. Chen, *ACS Nano*, 2018, **12**, 9596–9607.

48   W. Niu, H. Chen, R. Chen, J. Huang, A. Palaniappan, H. Sun, B. G. Liedberg and A. I. Y. Tok, *Small*, 2014, **10**, 3637–3643.

49   P. Li, Y. Yan, B. Chen, P. Zhang, S. Wang, J. Zhou, H. Fan, Y. Wang and X. Huang, *Biomater. Sci.*, 2018, **6**, 877–884.

50   W. Wei, T. He, X. Teng, S. Wu, L. Ma, H. Zhang, J. Ma, Y. Yang, H. Chen, Y. Han, H. Sun and L. Huang, *Small*, 2012, **8**, 2271–2276.

51   Y. Wang, H. Wang, D. Liu, S. Song, X. Wang and H. Zhang, *Biomaterials*, 2013, **34**, 7715–7724.

52   M. Franco, V. Correia, P. Marques, F. Sousa, R. Silva, B. R. Figueiredo, A. Bernardes, R. P. Silva, S. Lanceros-Mendez and P. Costa, *Adv. Mater. Interfaces*, 2021, **8**, 2100578.

53   M. Franco, R. Alves, N. Perinka, C. Tubio, P. Costa and S. Lanceros-Mendéz, *ACS Appl. Electron. Mater.*, 2020, **2**, 2857–2867.

54   C. Rebelo, T. Reis, J. Guedes, C. Saraiva, A. F. Rodrigues, S. Simões, L. Bernardino, J. Peça, S. L. C. Pinho and L. Ferreira, *Nat. Commun.*, 2022, **13**, 4135.

55   C. Homann, L. Krukewitt, F. Frenzel, B. Grauel, C. Würth, U. Resch-Genger and M. Haase, *Angew. Chemie Int. Ed.*, 2018, **57**, 8765–8769.

56   R. F. Simões, R. Ferrão, M. R. Silva, S. L. C. Pinho, L. Ferreira, P. J. Oliveira and T. Cunha-Oliveira, *Food Chem. Toxicol.*, 2021, **149**, 111967.

57   M. L. DiFrancesco, E. Colombo, E. D. Papaleo, G. Manfredi, G. Lanzani and F. Benfenati, *Carbon N. Y.*, 2020, **162**, 308–317.

58   K. Wang, H. A. Fishman, H. Dai and J. S. Harris, *Nano Lett.*, 2006, **6**, 2043–2048.

59   F. Liu and D. Xue, *Chem. - A Eur. J.*, 2013, **19**, 10716–10722.

60   N. M. Gabor, J. C. W. Song, Q. Ma, N. L. Nair, T. Taychatanapat, K. Watanabe, T. Taniguchi, L. S. Levitov and P. Jarillo-Herrero, *Science (80-.).*, 2011, **334**, 648–652.

61   R. Raveendran-Nair, P. Blake, A. N. Grigorenko, K. S. Novoselov, T. J. Booth, T. Stauber, N. M. R. Peres and A. K. Geim, *Science (80-.).*, 2008, **320**, 1308.

62   K. F. Mak, M. Y. Sfeir, Y. Wu, C. H. Lui, J. A. Misewich and T. F. Heinz, *Phys. Rev. Lett.*, 2008, **101**, 196405.

63   D. Kuzum, H. Takano, E. Shim, J. C. Reed, H. Juul, A. G. Richardson, J. De Vries, H. Bink, M. A. Dichter, T. H. Lucas, D. A. Coulter, E. Cubukcu and B. Litt, *Nat. Commun.*, 2014, **5**, 5259.

64   C. Boehler, S. Carli, L. Fadiga, T. Stieglitz and M. Asplund, *Nat. Protoc.*, 2020, **15**, 3557–3578.

65   N. O. Laschuk, E. B. Easton and O. V. Zenkina, *RSC Adv.*, 2021, 11, 27925–27936.

66   M. Haase and H. Schäfer, *Angew. Chemie Int. Ed.*, 2011, **50**, 5808–5829.

67   E. M. Chan, G. Han, J. D. Goldberg, D. J. Gargas, A. D. Ostrowski, P. J. Schuck, B. E. Cohen and D. J. Milliron, *Nano Lett.*, 2012, **12**, 3839–3845.

68   F. Auzel, *Chem. Rev.*, 2004, **104**, 139–174.

69   L. M. Wiesholler, F. Frenzel, B. Grauel, C. Würth, U. Resch-Genger and T. Hirsch, *Nanoscale*, 2019, **11**, 13440–13449.

70   X. Xie, N. Gao, R. Deng, Q. Sun, Q. H. Xu and X. Liu, *J. Am. Chem. Soc.*, 2013, **135**, 12608–12611.

71   F. Wang, Y. Han, C. S. Lim, Y. Lu, J. Wang, J. Xu, H. Chen, C. Zhang, M. Hong and X. Liu, *Nature*, 2010, **463**, 1061–1065.

72   T. Cong, Y. Ding, S. Xin, X. Hong, H. Zhang and Y. Liu, *Langmuir*, 2016, **32**, 13200–13206.

73   S. Fischer, N. D. Bronstein, J. K. Swabeck, E. M. Chan and A. P. Alivisatos, *Nano Lett.*, 2016, **16**, 7241–7247.

74   R. Parameswaran, J. L. Carvalho-De-Souza, Y. Jiang, M. J. Burke, J. F. Zimmerman, K. Koehler, A. W. Phillips, J. Yi, E. J. Adams, F. Bezanilla and B. Tian, *Nat. Nanotechnol.*, 2018, **13**, 260–266.

75   R. Parameswaran, K. Koehler, M. Y. Rotenberg, M. J. Burke, J. Kim, K. Y. Jeong, B. Hissa, M. D. Paul, K. Moreno, N. Sarma, T. Hayes, E. Sudzilovsky, H. G. Park and B. Tian, *Proc. Natl. Acad. Sci.*, 2019, **116**, 413–421.

76   M. Tang, X. Zhang, A. Yang, Y. Liu, K. Xie, Y. Zhou, C. Wang, J. Liu, P. Shi and X. Lin, *Small*, 2022, **18**, 2105388.

77   H. U. Lee, S. Y. Park, S. C. Lee, S. Choi, S. Seo, H. Kim, J. Won, K. Choi, K. S. Kang, H. G. Park, H. S. Kim, H. R. An, K. H. Jeong, Y. C. Lee and J. Lee, *Small*, 2016, **12**,
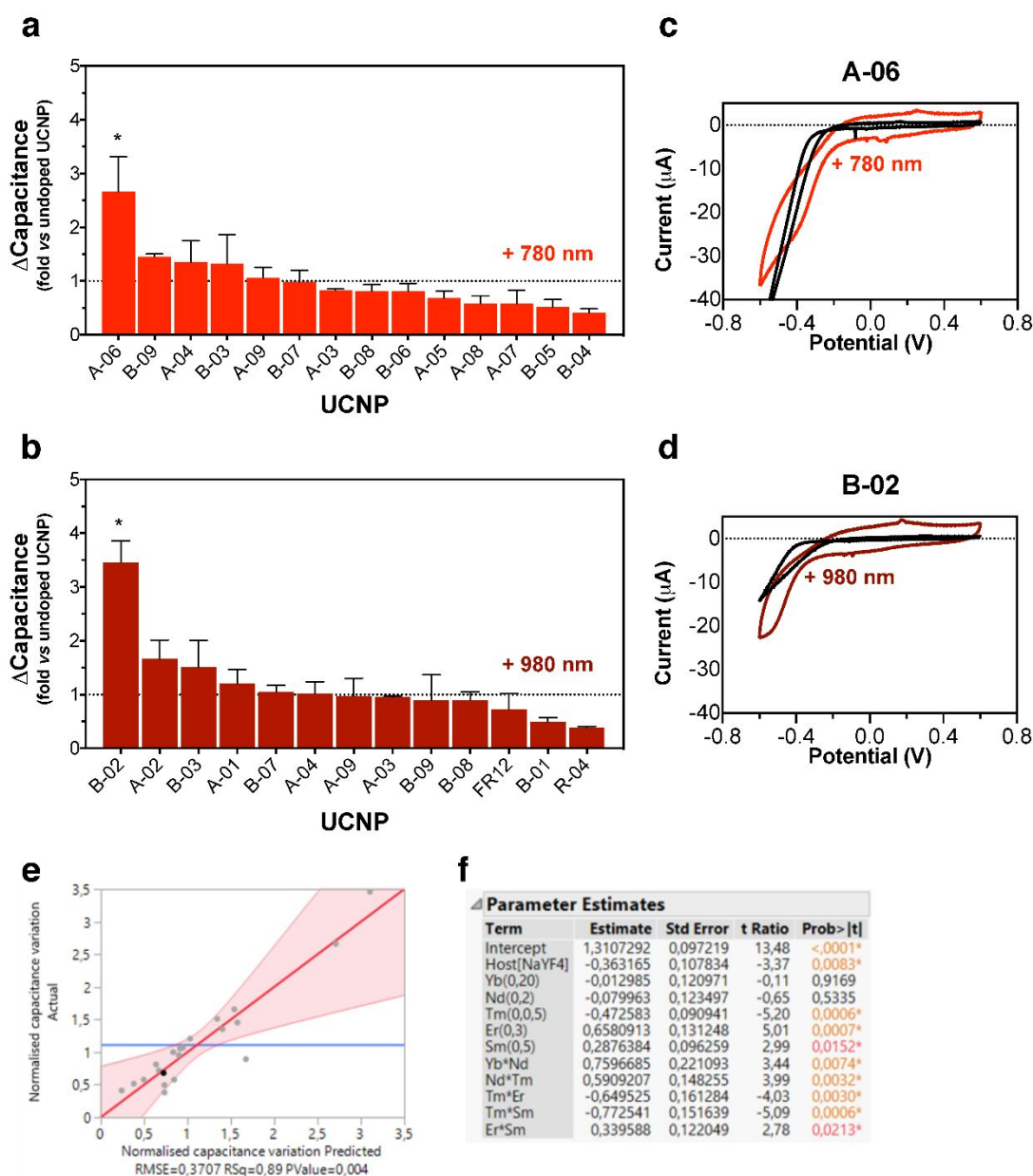
214–219.

78   I. A. Vacchi, J. Raya, A. Bianco and C. Ménard-Moyon, *2D Mater.*, 2018, **5**, 035037.

79   A. F. Rodrigues, L. Newman, N. Lozano, S. P. Mukherjee, B. Fadeel, C. Bussy and K. Kostarelos, *2D Mater.*, 2018, **5**, 035020.

80   J. S. Lee, A. Lipatov, L. Ha, M. Shekhirev, M. N. Andalib, A. Sinitskii and J. Y. Lim, *Biochem. Biophys. Res. Commun.*, 2015, **460**, 267–273.

81   M. Tang, Q. Song, N. Li, Z. Jiang, R. Huang and G. Cheng, *Biomaterials*, 2013, **34**, 6402–6411.

82   S. B. Yoon, G. Lee, S. B. Park, H. Cho, J. O. Lee and B. Koh, *RSC Adv.*, 2020, **10**, 19382–19389.

83   O. Akhavan and E. Ghaderi, *J. Mater. Chem. B*, 2014, **2**, 5602.

84   O. Akhavan, E. Ghaderi and S. A. Shirazian, *Colloids Surfaces B Biointerfaces*, 2015, **126**, 313–321.

85   J. Kovalevich and D. Langford, *Methods Mol. Biol.*, 2013, **1078**, 9–21.

86   H. Xicoy, B. Wieringa and G. J. M. Martens, *Mol. Neurodegener.*, 2017, **12**, 10.

87   L. Agholme, T. Lindström, K. Kgedal, J. Marcusson and M. Hallbeck, *J. Alzheimer's Dis.*, 2010, **20**, 1069–1082.

88   D. McManus, S. Vranic, F. Withers, V. Sanchez-Romaguera, M. Macucci, H. Yang, R. Sorrentino, K. Parvez, S.-K. Son, G. Iannaccone, K. Kostarelos, G. Fiori and C. Casiraghi, *Nat. Nanotechnol.*, 2017, **12**, 343–350.

89   S. Vranic, A. F. Rodrigues, M. Buggio, L. Newman, M. R. H. White, D. G. Spiller, C. Bussy and K. Kostarelos, *ACS Nano*, 2018, **12**, 1373–1389.

90   F. Xiaoli, Z. Yaqing, L. Ruhui, L. Xuan, C. Aijie, Z. Yanli, H. Chen, C. Lili and S. Longquan, *J. Hazard. Mater.*, 2021, **416**, 126158.

91   T. Santos, R. Ferreira, E. Quartin, C. Boto, C. Saraiva, J. Bragança, J. Peça, C. Rodrigues, L. Ferreira and L. Bernardino, *Acta Biomater.*, 2017, **59**, 293–302.

92   D. A. Bórquez, P. J. Urrutia, C. Wilson, B. Van Zundert, M. T. Núñez and C. González-Billault, *J. Neurochem.*, 2016, **137**, 506–517.

93   T. Prozorovski, R. Schneider, C. Berndt, H. P. Hartung and O. Aktas, *Biochim. Biophys. Acta - Gen. Subj.*, 2015, 1850, 1543–1554.

94   A. A. Dayem, B. Kim, S. Gurunathan, H. Y. Choi, G. Yang, S. K. Saha, D. Han, J. Han, K. Kim, J. H. Kim and S. G. Cho, *Biotechnol. J.*, 2014, **9**, 934–943.

95   A. M. Brown, F. C. Riddoch, A. Robson, C. P. F. Redfern and T. R. Cheek, *Biochem. J.*, 2005, **388**, 941–948.

96   M. Seo, Y. Kim, Y. Il Lee, S. Y. Kim, Y. M. Ahn, U. G. Kang, M. S. Roh, Y. S. Kim and Y. S. Juhnn, *Neurosci. Lett.*, 2006, **404**, 87–92.

97   X. B. He, S. H. Yi, Y. H. Rhee, H. Kim, Y. M. Han, S. H. Lee, H. Lee, C. H. Park, Y. S. Lee, E. Richardson, B. W. Kim and S. H. Lee, *Stem Cells*, 2011, **29**, 1861–1873.

98   K. A. Tennant, S. L. Taylor, E. R. White and C. E. Brown, *Nat. Commun.*, 2017, **8**, 15879.

99   A. S. Wahl, U. Büchler, A. Brändli, B. Brattoli, S. Musall, H. Kasper, B. V. Ineichen, F. Helmchen, B. Ommer and M. E. Schwab, *Nat. Commun.*, 2017, **8**, 1187.

100   X. Feng, J. Guo, H. C. Sigmon, R. P. Sloan, A. M. Brickman, F. A. Provenzano and S. A. Small, *PLoS One*, 2020, **15**, e0234255.

101   R. Qazi, A. M. Gomez, D. C. Castro, Z. Zou, J. Y. Sim, Y. Xiong, J. Abdo, C. Y. Kim, A. Anderson, F. Lohner, S. H. Byun, B. Chul Lee, K. I. Jang, J. Xiao, M. R. Bruchas and J. W. Jeong, *Nat. Biomed. Eng.*, 2019, **3**, 655–669.

102   C. Saraiva, J. Paiva, T. Santos, L. Ferreira and L. Bernardino, *J. Control. Release*, 2016, **235**, 291–305.

103   A. M. L. Piloto, D. S. M. Ribeiro, S. S. M. Rodrigues, J. L. M. Santos and M. G. Ferreira Sales, *Sensors Actuators B Chem.*, 2020, **304**, 127343.

104   M. Liu, J. Wei, Y. Wang, H. Ouyang and Z. Fu, *Talanta*, 2019, **195**, 706–712.

105   A. D. Ostrowski, E. M. Chan, D. J. Gargas, E. M. Katz, G. Han, P. J. Schuck, D. J. Milliron and B. E. Cohen, *ACS Nano*, 2012, **6**, 2686–2692.

106   P. Pereira, D. P. Ferreira, J. C. Araújo, A. Ferreira and R. Fangueiro, *Polymers (Basel).*, 2020, **12**, 2189.

Figure 1. Electrochemical characterization of screen-printed graphene electrodes. (a) Representative cyclic voltammetry (CV) curves of graphene electrodes exposed to light at different wavelengths (405, 780, 980 nm) using a fixed laser power (60 mW cm⁻²). **(b)** Cathodic charge storage capacity (CSC) was calculated by integration of the negative sweep (area below the dashed line in the CV curve. Results are expressed as mean ± SEM (n = 3). One-way ANOVA with *post hoc* Tukey's multiple comparisons test was performed: **(*),** $p < 0.05$. **(c)** Representative Bode plots of graphene electrodes exposed to light at a laser
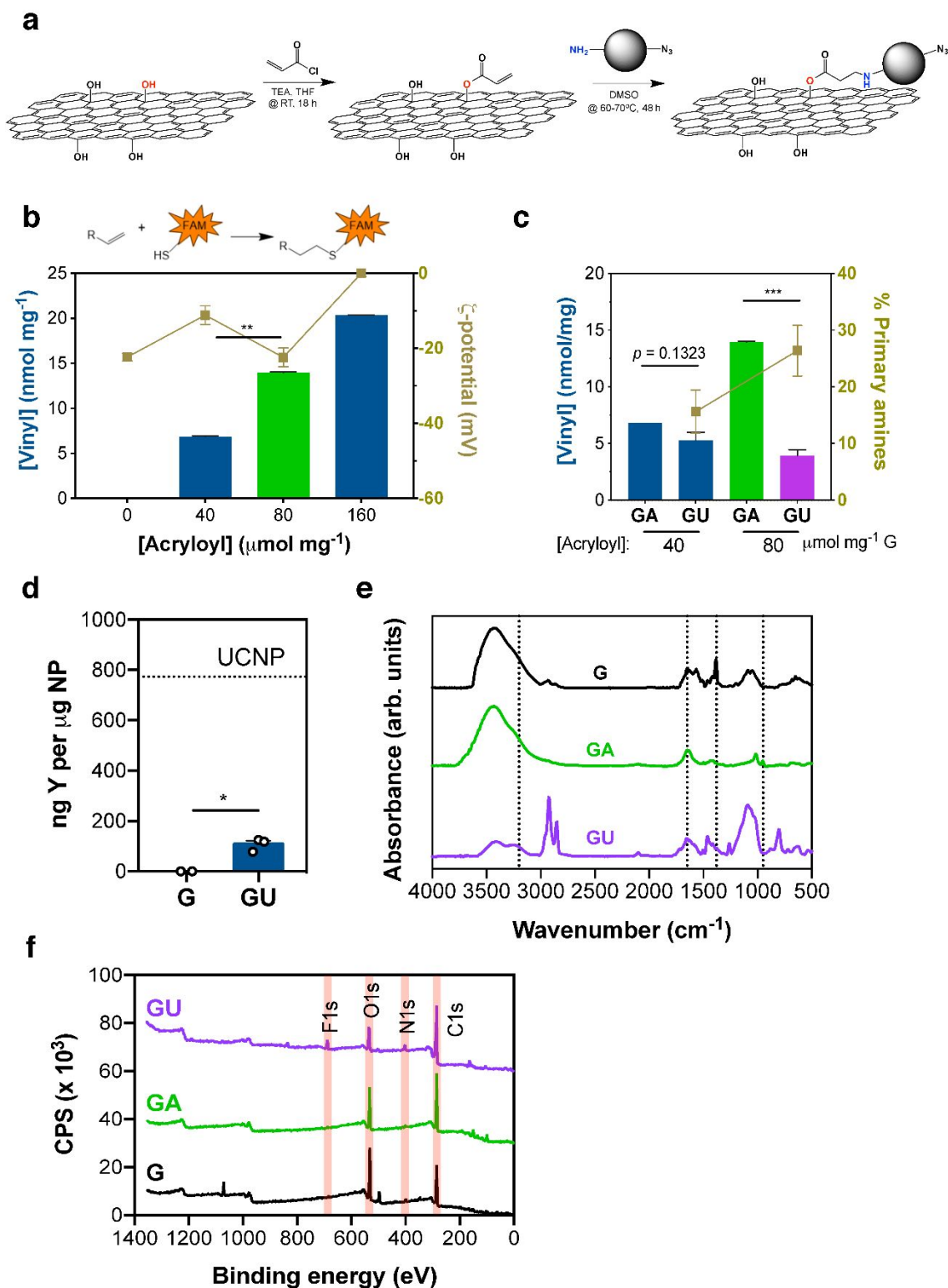
power of 60 mW cm^{-2}. Dashed line corresponds to a -45° phase angle, in order to determine at which frequency the electrode becomes capacitive. **(d)** Variation in impedance induced by light was compared at different frequencies. Results are expressed as mean ± SEM (n = 3). Two-way ANOVA with *post hoc* Dunnett's multiple comparisons test against non-irradiated electrodes was performed: **(*)**, *p* < 0.05; **(**)**, *p* < 0.01. **(e)** Representative CV curves of graphene electrodes exposed to NIR radiation at λ = 780 nm, using different irradiances. **(f)** CSC and **(g)** capacitance increased with laser power following a logarithmic function (**g**, inset). **(h)** Electrode photosensitivity to NIR radiation at λ = 780 nm was also modelled by a logarithmic function.

Figure 2. Effect of UCNP composition on the electrical conductivity of graphene electrodes after NIR activation. UCNPs were drop-casted onto graphene electrodes and their electrochemical response to NIR radiation (30 mW cm^{-2}) was measured by CV. Only one candidate was identified after irradiation at **(a)**
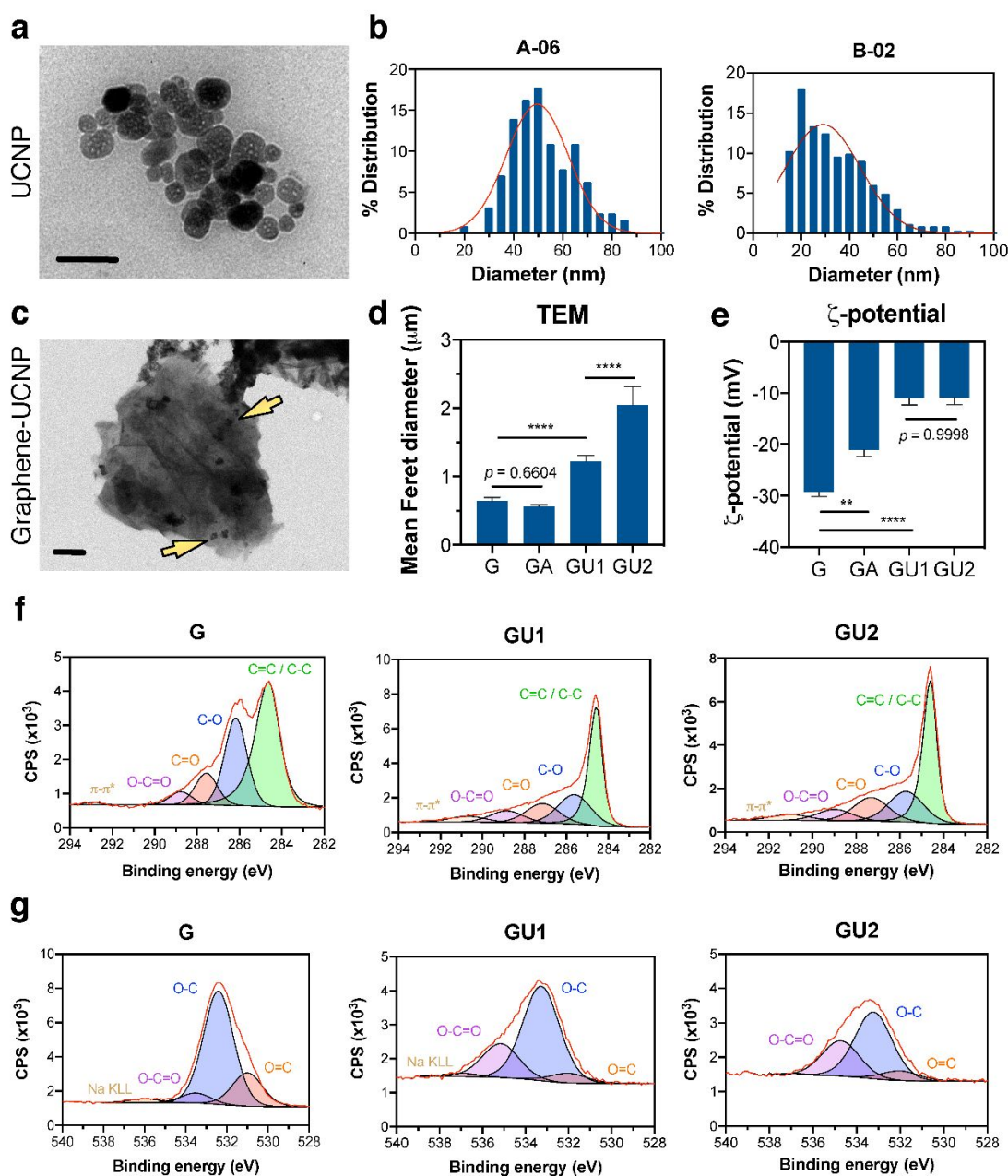
λ = 780 nm and **(b)** λ = 980 nm, showing a statistically significant increase in capacitance following NIR exposure against pure $NaYF_4$ nanocrystals lacking lanthanide dopants (dashed lines). Results are expressed as mean ± SEM (n = 2-3). For each wavelength, one-way ANOVA with *post hoc* Tukey's multiple comparisons test was performed: **(*),** $p < 0.05$. **(c)** Representative CV curves of lead candidates with (red) or without (black) exposure to NIR radiation at λ = 780 nm or **(d)** λ = 980 nm. **(e)** The highest variation in capacitance obtained with NIR radiation (λ = 780 or 980 nm) was correlated with UCNP composition by multivariate analysis. **(f)** List of parameters used in predictive model after eliminating statistically insignificant ($p > 0.05$) parameters one-by-one. Insignificant parameters in the model were maintained due to significant first-order interactions between lanthanides.
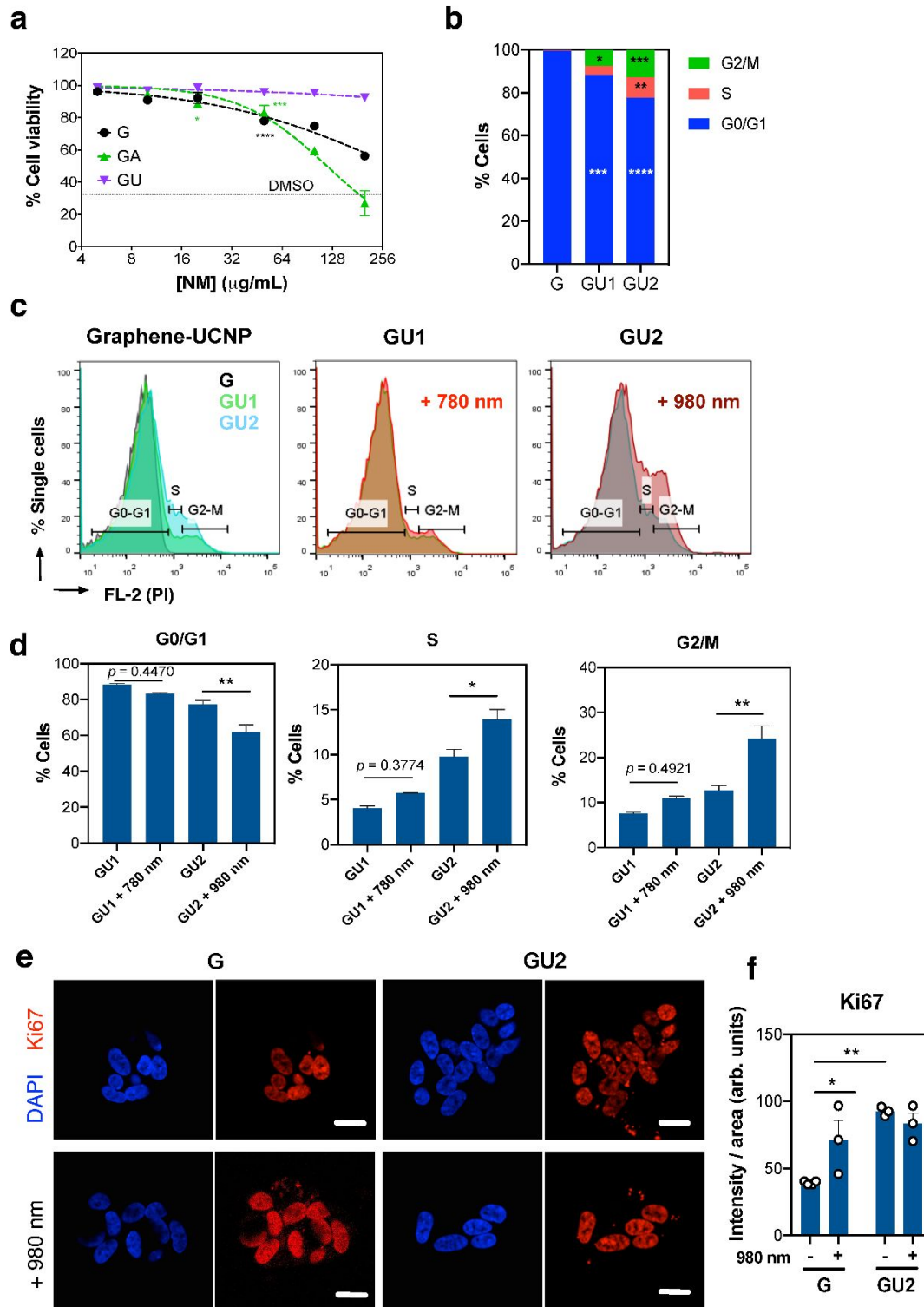
Figure 3. Conjugation of graphene nanoplatelets with UCNPs. (a) Graphene-UCNP composites were produced via Michael addition, following acrylation of graphene nanoplatelets. **(b)** Quantification of vinyl groups introduced by acrylation was performed using a fluorescent probe targeting these moieties via thiol-Michael click reaction. Optimization of reaction conditions aimed to maximize the abundance of vinyl groups without impacting the colloidal stability of acrylated graphene. Optimal condition was highlighted with a

green bar. Results are expressed as mean ± SEM (n = 3). Two-way ANOVA with *post hoc* Dunnett's multiple comparisons test against non-irradiated electrodes was performed: **(**)**, $p < 0.01$. **(c)** Quantification of vinyl and primary amines in acrylated graphene (GA) and the resulting graphene-UCNP composites (GU) was performed to optimize the immobilization of silane-coated UCNPs (estimated by amine content). The introduced vinyl groups after acrylation were reactive towards the primary amines of UCNP (~63 groups per UCNP). The selected dose of 80 μmol acryloyl chloride mg^{-1} graphene underwent a significant reduction in vinyl content and exhibited a greater content of primary amines, suggesting the efficient conjugation of UCNPs. Vinyl content was assessed by two-way ANOVA with *post hoc* Sidak's multiple comparisons test: **(***)**, $p < 0.001$. **(d)** Quantification of yttrium (Y) by ICP-MS in graphene nanoplatelets before (G) and after immobilization of UCNPs (GU). Results are expressed as mean ± SEM (n = 2-3). Two-tailed unpaired t test was performed: **(*)**, $p < 0.05$**.** The yield of conjugation of UCNPs to graphene nanoplatelets was represented by the estimated amount of UCNPs in each sample, which was derived by dividing the obtained amount of Y per mass of lyophilized sample by the value obtained for pure UCNPs (773.1 ± 16.5 ng Y $μg^{-1}$ UCNP). **(e)** FTIR spectra of graphene nanoplatelets (G), acrylated graphene (GA), and graphene-UCNP (GU) describe the modifications in surface chemistry of graphene throughout the reaction steps. Dashed lines at 1650 cm^{-1} and 1380 cm^{-1} highlight the contributions of aromatic carbon and phenol groups, respectively, demonstrating the selectivity of the acrylation reaction toward hydroxyl groups. The reaction of vinyl groups with primary amines of UCNPs was demonstrated by the disappearance of the peak at 950 cm^{-1} alongside the emergence of a shoulder around 3200 cm^{-1}, indicative of secondary amines. **(f)** XPS survey spectra of GBMs highlighting the changes in carbon and oxygen content, as well as the introduction of nitrogen and fluorine from UCNPs.
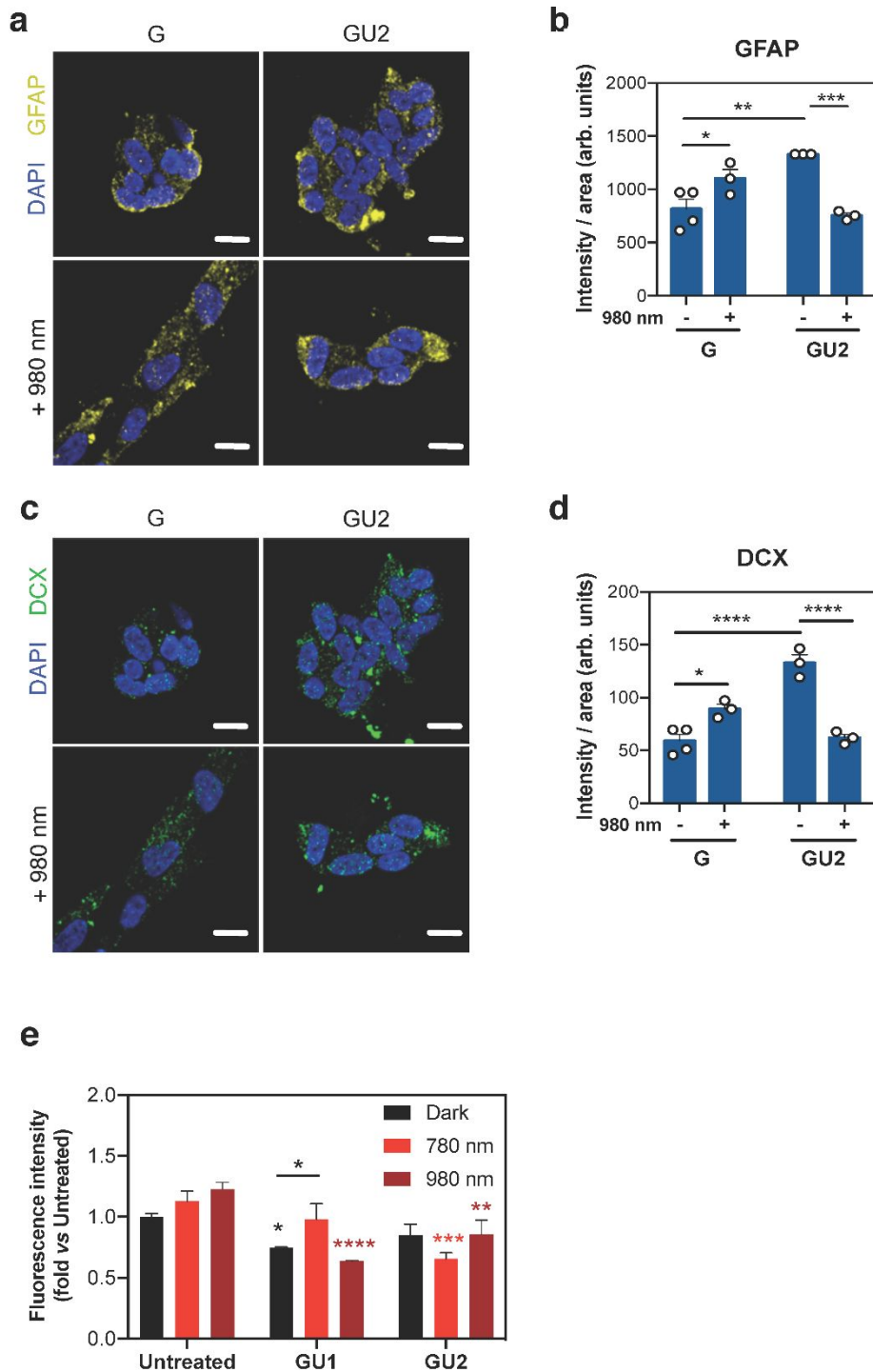
Figure 4. Characterization of graphene-UCNP nanocomposites. (a) Representative TEM image of B-02 UCNPs. Scale bar = 100 nm. **(b)** Size distributions of lead UCNP formulations A-06 and B-02 were fitted to a Gaussian distribution. **(c)** Representative TEM image of GU2 illustrates the attachment of small UCNP clusters (highlighted with yellow arrows), following the conjugation of B-02 UCNPs to graphene nanoplatelets. Scale bar = 1 μm. **(d)** Average particle size was determined by manually measuring the longest Feret diameter of >100 NPs. **(e)** Surface charge of GBMs determined by ζ-potential. Results are expressed as mean ± SEM (n = 5). In **(d)** and **(e)**, one-way ANOVA with Tukey's multiple comparisons test was performed: **(**)**, $p < 0.01$; **(****)**, $p < 0.0001$. **(f)** High-resolution C1s and **(g)** O1s spectra of graphene nanoplatelets before (G) and after conjugation with UCNPs (GU1 and GU2).

Figure 5. Impact of graphene-UCNP nanocomposites on the proliferation of SH-SY5Y neuroblastoma cells. (a) Viability of SH-SY5Y cells was assessed 24 h after treatment with GBMs by determining the percentage of PI-stained cells using high-content imaging. Cells were treated with GBMs and UCNPs over a range of concentrations (5 – 200 µg mL^{-1}). DMSO (10% v/v) was used as a positive control. Results are expressed as mean ± SEM (n = 3). Two-way ANOVA with *post hoc* Dunnett's multiple comparisons test against the untreated control was performed: **(*)**, $p < 0.05$; **(***)**, $p < 0.001$; **(****)**, $p <$

0.0001. **(b)** Effect of GBM substrate and NIR radiation (100 mW cm^{-2}, 5 min) on cell cycle of PI-stained SH-SY5Y cells was determined by flow cytometry. **(c)** Conjugation of UCNPs with graphene nanoplatelets significantly increased the number of cells in the G2/M of the cell cycle and decreased the number of cells in G0/G1. Results are expressed as mean ± SEM (n = 3). Two-way ANOVA with *post hoc* Tukey's multiple comparisons test was performed: **(*),** $p < 0.05$; **(**)**, $p < 0.01$; **(***)**, $p < 0.001$; **(****)**, $p < 0.0001$. **(d)** Effect of NIR radiation in each graphene-UCNP nanocomposite was evaluated by comparing cell populations in G0/G1, S, and G2/M phases of the cell cycle. Results are expressed as mean ± SEM (n = 3). One-way ANOVA with *post hoc* Tukey's multiple comparisons test was performed: **(*),** $p < 0.05$; **(**)**, $p < 0.01$. **(e)** Representative immunofluorescence images of Ki67 expression in SH-SY5Y cells cultured on graphene-based substrates with or without exposure to NIR radiation at λ = 980 nm (100 mW cm^{-2}, 5 min). Scale bars = 10 μm. **(f)** While NIR activation at λ = 980 nm increased the expression of Ki67 in cells cultured on graphene substrates (G), it was unaltered in cells cultured on graphene-UCNP substrates (GU2). Results are expressed as mean ± SEM (n = 3-4). Two-way ANOVA with *post hoc* Sidak's multiple comparisons test was performed: **(*),** $p < 0.05$; **(**)**, $p < 0.01$.

Figure 6. Impact of graphene-UCNP nanocomposites on the differentiation of SH-SY5Y neuroblastoma cells. SH-SY5Y cells cultured on graphene-based substrates and exposed to NIR radiation at λ = 980 nm (100 mW cm^{-2}, 5 min). **(a)** Representative immunofluorescence images of GFAP (yellow) and **(b)** quantification of GFAP expression. **(c)** Representative immunofluorescence images of DCX (green) and **(d)** quantification of DCX expression. While NIR activation at λ = 980 nm increased the expression of GFAP and DCX and Ki67 in cells cultured on graphene substrates (G), the expression of GFAP and DCX significantly decreased in cells cultured on graphene-UCNP substrates (GU2). In **(a)** and

(c), scale bars = 10 µm. In **(b)** and **(d)**, results are expressed as mean ± SEM (n = 3-4). Two-way ANOVA with *post hoc* Sidak's multiple comparisons test was performed: **(**),** $p < 0.01$; **(***)**, $p < 0.001$; **(****)**, $p < 0.0001$. **(e)** Intracellular ROS production in SH-5YSY cells was measured 4 h after treatment with GU1 or GU2 in suspension (100 µg mL^{-1}), followed by exposure to NIR radiation at λ = 780 nm or λ = 980 nm (100 mW cm^{-2}) for 5 min. Results are expressed as mean ± SEM (n = 3). Two-way ANOVA with *post hoc* Tukey's multiple comparisons test was performed: **(*),** $p < 0.05$; **(**)**, $p < 0.01$; **(***)**, $p < 0.001$; **(****)**, $p < 0.0001$.